JGR Space Physics

RESEARCH ARTICLE
10.1029/2022JA030580

Geomagnetic Disturbances That Cause GICs: Investigating Their Interhemispheric Conjugacy and Control by IMF Orientation

Mark J. Engebretson[1], Laura E. Simms[1,2], Viacheslav A. Pilipenko[1,3], Lilia Bouayed[1,4], Mark B. Moldwin[2], James M. Weygand[5], Michael D. Hartinger[6], Zhonghua Xu[7], C. Robert Clauer[7], Shane Coyle[7], Anna N. Willer[8], Mervyn P. Freeman[9], and Andy J. Gerrard[10]

[1]Department of Physics, Augsburg University, Minneapolis, MN, USA, [2]Department of Climate and Space Sciences and Engineering, University of Michigan, Ann Arbor, MI, USA, [3]Space Research Institute, Moscow, Russia, [4]Now at Department of Physics, University of Minnesota, Minneapolis, MN, USA, [5]Department of Earth, Planetary, and Space Sciences, University of California, Los Angeles, CA, USA, [6]Space Science Institute, Boulder, CO, USA, [7]Bradley Department of Electrical and Computer Engineering, Virginia Polytechnic Institute and State University, Blacksburg, VA, USA, [8]DTU Space, Kongens Lyngby, Denmark, [9]British Antarctic Survey, Cambridge, UK, [10]Department of Physics, New Jersey Institute of Technology, Newark, NJ, USA

Abstract Nearly all studies of impulsive geomagnetic disturbances (GMDs, also known as magnetic perturbation events MPEs) that can produce dangerous geomagnetically induced currents (GICs) have used data from the northern hemisphere. In this study, we investigated GMD occurrences during the first 6 months of 2016 at four magnetically conjugate high latitude station pairs using data from the Greenland West Coast magnetometer chain and from Antarctic stations in the conjugate AAL-PIP magnetometer chain. Events for statistical analysis and four case studies were selected from Greenland/AAL-PIP data by detecting the presence of >6 nT/s derivatives of any component of the magnetic field at any of the station pairs. For case studies, these chains were supplemented by data from the BAS-LPM chain in Antarctica as well as Pangnirtung and South Pole in order to extend longitudinal coverage to the west. Amplitude comparisons between hemispheres showed (a) a seasonal dependence (larger in the winter hemisphere), and (b) a dependence on the sign of the *By* component of the interplanetary magnetic field (IMF): GMDs were larger in the north (south) when IMF *By* was >0 (<0). A majority of events occurred nearly simultaneously (to within ±3 min) independent of the sign of *By* as long as $|By| \leq 2\,|Bz|$. As has been found in earlier studies, IMF *Bz* was <0 prior to most events. When IMF data from Geotail, Themis B, and/or Themis C in the near-Earth solar wind were used to supplement the time-shifted OMNI IMF data, the consistency of these IMF orientations was improved.

Key Points:

- Large (>6 nT/s) geomagnetic disturbances (GMDs) were identified in data from conjugate magnetometer arrays in Greenland and Antarctica
- GMD amplitudes were larger in the winter hemisphere and larger in the north (south) when interplanetary magnetic field *By* was >0 (<0)
- Minima in the *Bx* component of most GMDs appeared simultaneously (within 3 min) in conjugate hemispheres

Supporting Information:

Supporting Information may be found in the online version of this article.

Correspondence to:

M. J. Engebretson,
engebret@augsburg.edu

Citation:

Engebretson, M. J., Simms, L. E., Pilipenko, V. A., Bouayed, L., Moldwin, M. B., Weygand, J. M., et al. (2022). Geomagnetic disturbances that cause GICs: Investigating their interhemispheric conjugacy and control by IMF orientation. *Journal of Geophysical Research: Space Physics*, *127*, e2022JA030580. https://doi.org/10.1029/2022JA030580

Received 22 APR 2022
Accepted 28 SEP 2022

Author Contributions:

Conceptualization: Mark J. Engebretson, Michael D. Hartinger
Data curation: Mark J. Engebretson, Mark B. Moldwin, Michael D. Hartinger, C. Robert Clauer, Anna N. Willer, Mervyn P. Freeman, Andy J. Gerrard
Formal analysis: Mark J. Engebretson, Laura E. Simms, Viacheslav A. Pilipenko, James M. Weygand, Shane Coyle
Funding acquisition: Mark J. Engebretson

1. Introduction

This study continues our efforts to identify physical factors associated with geomagnetic disturbances (GMDs, also known as magnetic perturbation events MPEs)—solitary perturbations of 5–10 min duration and amplitudes of hundreds (or more) nT—that are known to be causally related to geomagnetically induced currents (GICs) that can damage power grids and pipeline systems as a result of their rapid changes of magnetic field. GICs are one of the many phenomena included in the field of space weather; extreme space weather events are now recognized as a serious threat to worldwide technological infrastructure (Boteler et al., 1998), and efforts to document, understand, and eventually predict them are under way in many nations around the world (e.g., Knipp & Gannon, 2019). Observations of the extreme geomagnetic storms of May 1921 and March 1989 and their effects, including large GICs, have been reported by Boteler (2019), Hapgood (2019), and Love et al. (2019). Knipp (2015) presented an annotated bibliography of studies of GICs, and Ngwira and Pulkkinen (2019) provided a list of recent studies of GIC events as part of a Geophysical Monograph on GICs and their impacts on power systems (Gannon et al., 2019).

As Woodroffe et al. (2016) noted, "An oft-cited threshold for magnetic induction hazards is $\dot{B} = 5$ nT/s (e.g., Boteler, 2001; Molinski et al., 2000)." This study uses a slightly higher threshold of 6 nT/s, so the identified events are well above the "danger" threshold. Both isolated GMDs and extended intervals of GMDs can be

Investigation: Mark J. Engebretson, Lilia Bouayed, James M. Weygand, Zhonghua Xu
Methodology: Mark J. Engebretson, James M. Weygand, Michael D. Hartinger

damaging; in some cases cumulative effects can lead up to damage that is finally triggered by isolated events (Marshall et al., 2011).

Nearly all prior studies of GMDs have used northern hemisphere data. This is especially appropriate at high latitudes: large populations in Northern Europe are affected by GICs, but there are no large populations at high latitudes in the southern hemisphere, and Antarctica has only very sparse magnetometer coverage. However, because perturbations of the ionospheric plasma in the northern hemisphere depend in part on the ionospheric conductivity in both hemispheres and on the plasma/driving conditions along the entire length of magnetic field lines connecting them, interhemispheric comparisons are needed to fully validate theories and models of GMDs, whether in the northern or southern hemisphere.

A set of four case studies by Engebretson et al. (2020) comparing GMDs observed in latitudinally extended magnetometer arrays at magnetically conjugate high latitude locations in the Arctic (Greenland and eastern Canada) and Antarctica found that these nighttime GMD events appeared within a few minutes of each other at stations in opposite hemispheres but with similar magnetic latitudes. These events occurred under a wide range of geomagnetic conditions, but common to each was a negative interplanetary magnetic field *Bz* that often exhibited at least a modest increase at or near the time of the event. This study also noted that the GMD amplitude was largest in the winter hemisphere during three of the four intervals presented, and concluded, using these data along with models of ionospheric conductances, that GMDs corresponded better to driving by a current generator model than by a voltage generator model. IMF orientations dominated by large *By* components are known to cause some nonconjugate magnetospheric and ionospheric effects at high latitudes, but the effect of IMF *By* on GMDs was not addressed in this earlier study.

In a more recent superposed epoch study, Engebretson, Ahmed et al. (2021) reported that the medians of nearly all the nearly 700 $\geq$ 6 nT/s GMDs observed at five stations in Arctic Canada during 2015 and 2017, both premidnight and postmidnight, were preceded by intervals of negative IMF *Bz*. This pattern held for the 25th and 75th percentile traces in most cases as well, but not every *Bz* trace was negative prior to GMD occurrence or showed a similar time dependence. This paper also included work comparing a set of 156 intervals during 2015 compiled by Shane Coyle of Virginia Tech when the IMF vector was within $\pm$30° of the GSM *Y* axis, |*By*| was >6 nT, and events lasted longer than 30 min, to the times of 200 GMD occurrences at three stations in eastern Arctic Canada during that year. Only one of these GMDs occurred during the time of a large IMF *By* event. These results suggested that conditions strongly dominated by IMF *By* orientations may suppress the magnetotail instabilities that appear to be the cause of these events, but did not address the effect of moderate or zero IMF *By* conditions on GMDs or their conjugacy. This current study was begun with the intent to look for the influence of IMF *By* and possibly other factors that might affect the interhemispheric conjugacy of these events, using all nighttime GMDs with amplitudes $\geq$6 nT/s ($\geq$360 nT/min) that appeared in at least one station in magnetically conjugate subsets of these same Greenland and Antarctic arrays during the first 6 months of 2016.

In this study, we present four case studies as well as detailed information on a large number of GMDs observed in conjugate hemispheres. We can confirm our earlier findings that IMF B*y* polarity and seasonal effects cause hemispheric differences in amplitude, but even combined these are unable to account for the large variability in amplitude ratios, and we also demonstrate the near simultaneity of many of these events in both hemispheres. Section 2 describes the data used in this study and the procedures used to identify and quantify conjugate events. Section 3 presents four multistation case studies, and Section 4 presents statistical studies that focus on the relative amplitude and timing of these events. Section 5 discusses the implications of these observations, and Section 6 summarizes our findings.

2. Data Set and Analysis Methods

Northern hemisphere magnetometer data used in this study were recorded by the Greenland West Coast magnetometer chain (https://www.space.dtu.dk/MagneticGroundStations) and the MACCS array (https://doi.org/10.48322/sydj-ab90, Engebretson et al., 1995). Southern hemisphere data were recorded by the AAL-PIP magnetometer chain in Antarctica (Clauer et al., 2014), the British Antarctic Survey (BAS) Low Power Magnetometer chain (Kadokura et al., 2008), and the fluxgate magnetometer at South Pole Station, Antarctica (Engebretson et al., 1997; Lanzerotti et al., 1990). Data are presented in local magnetic coordinates. In the northern hemisphere (at MACCS and Greenland West Coast chain stations) and in the southern hemisphere (at AAL-PIP and BAS-LPM stations)

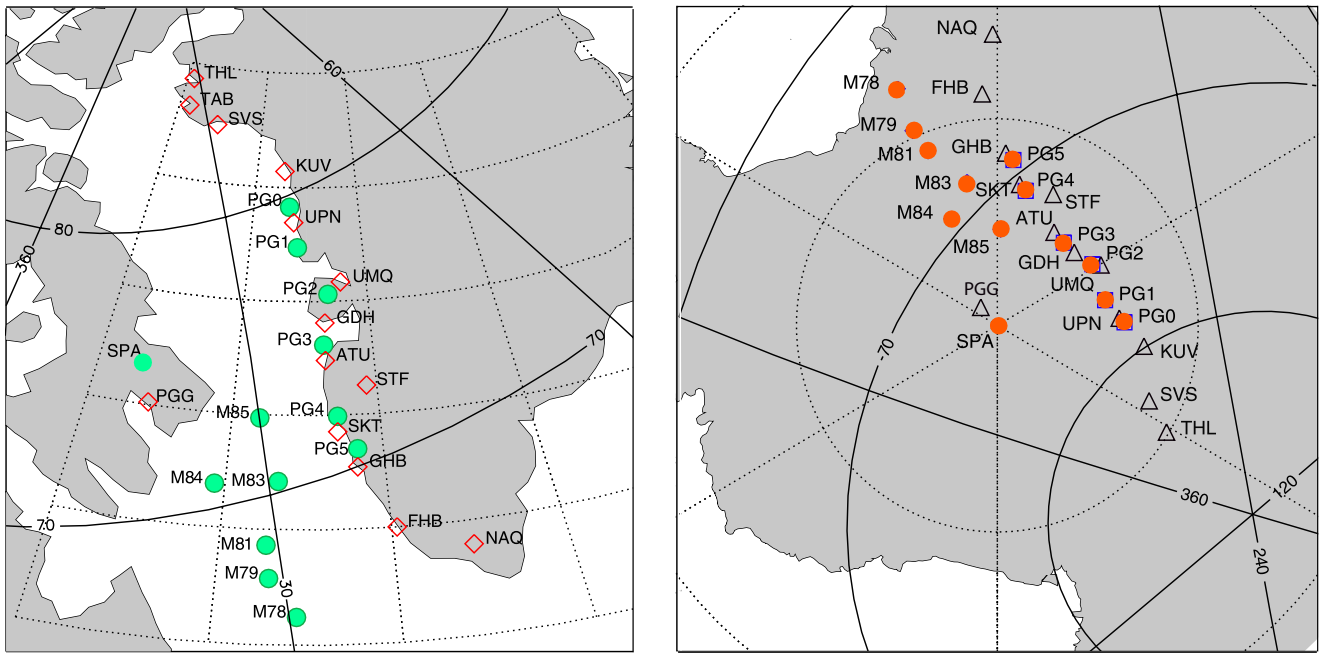

Figure 1. Maps showing the location of ground magnetometer stations used for this study. (a) Map of Arctic Canada and Greenland, showing stations in the northern hemisphere (open red diamonds) and the conjugate mapped locations of southern hemisphere stations (filled green circles). (b) Map of Antarctica, showing stations in the southern hemisphere (filled orange circles) and the conjugate mapped locations of northern hemisphere stations (open triangles). Solid lines show corrected geomagnetic coordinates. Conjugate mappings were based on the IGRF model magnetic field for epoch 2016 (https://omniweb.gsfc.nasa.gov/vitmo/cgm.html).

the sensor axes are oriented as follows: X: magnetic north, Y: magnetic east, and Z: vertically down. The South Pole magnetometer sensors are X: magnetic north, Y: magnetic east, and Z: vertically upward (a left-handed system). The sampling rate of MACCS data is 2 Hz, and for the other stations 1 Hz.

Figure 1 and Table 1 show that South Pole Station in Antarctica is in approximate magnetic conjugacy to MACCS station Pangnirtung in Canada. Figure 1 also shows that the six AAL-PIP stations in Antarctica, located about 20° farther east in corrected geomagnetic (CGM) longitude, are in close magnetic conjugacy to the middle of the Greenland West Coast chain, and that the BAS-LPM chain is conjugate in CGM magnetic latitude to several of the lower latitude Greenland West Coast stations, but approximately midway in CGM longitude between the Canadian and Greenland stations (Table 1).

The statistical part of this study is based on data from a subset of four stations in the equatorward part of the AAL-PIP array (PG2, PG3, PG4, and PG5) and four nearly conjugate stations ((UMQ, GDH, STF, and SKT, respectively) in the Greenland West Coast Chain. Data from 2016 were chosen for study because of the best AAL-PIP up-time during conditions of either active or moderate solar activity. The limitation to the first 6 months is a consequence of the power availability at the remote AAL-PIP stations. These are powered by solar cells and batteries, and at most of these stations the batteries discharged slightly more than halfway through the calendar year. For case studies data from these stations were supplemented by data from Pangnirtung, South Pole, and the three most poleward stations of the BAS-LPM Chain (M85, M84, and M83) in order to provide a modest extension of longitudinal coverage to the west but in the same range of MLAT. The separation in MLT of SPA from GDH and of PGG from STF is ~1.3 hr, and PGG is at a predominantly westward distance of 673 km from STF.

Full-day data from each of the stations in the four Greenland/AAL-PIP station pairs were analyzed to identify GMDs with amplitude ≥6 nT/s each day at each station. Events were selected and derivatives calculated using the semiautomatic procedure described by Engebretson, Pilipenko et al. (2019). This procedure began by displaying a daily magnetogram (a 24-hr three-axis plot of the magnetic field at each station) in local geomagnetic coordinates on a computer screen. Once a rapid (<20 min duration) and large amplitude (>~200 nT) magnetic perturbation was visually identified, the IDL cursor function was used to select times ~15–60 min before and after the perturbation in order to zoom in on the relatively short duration of the event and separate it from the times of other possible activity. The times and values of extrema in this interval were recorded for each component, and

Table 1
Magnetometer Stations Used in This Study

Northern hemisphere					Southern hemisphere				
Array	Geogr Lat	Geogr Lon	CGM Lat	CGM Lon	Array	Geogr Lat	Geogr Lon	CGM Lat	CGM Lon
MACCS									
Pangnirtung	66.1°	294.2°	73.2°	19.8°	South Pole	−90.00°	–	−74.5°	18.7°
					AAL-PIP				
Greenland Coastal Chain					PG0	−83.67°	88.68°	−78.5°	18.7°
THL	77.47°	290.77°	84.0°	26.4°	PG1	−84.50°	77.20°	−77.3°	37.3°
TAB	76.54°	291.18°	83.2°	25.0°	PG2	−84.42°	57.95°	−75.7°	39.1°
SVS	76.02°	294.90°	82.3°	30.4°	PG3	37.63°	−73.9°	36.7°	84.81°
KUV	74.57°	302.82°	80.0°	39.4°	PG4	−83.34°	12.25°	−71.2°	36.4°
UPN	72.78°	303.85°	78.2°	38.1°	PG5	−81.96°	5.71°	−69.9°	37.2°
UMQ	70.68°	307.87°	75.7°	40.8°					
GDH	69.25°	306.47°	74.5°	37.8°	British Antarctic Survey Low Power Magnetometer Chain				
ATU	67.93°	306.43°	73.2°	36.8°	M85-002	−85.36°	2.06°	−71.8°	30.1°
STF	67.02°	309.28°	71.9°	39.5°	M84-336	−84.36°	−23.85°	−69.8°	25.9°
SKT	65.42°	307.10°	70.7°	36.1°	M83-348	−82.90°	−12.25°	−69.2°	30.6°
GHB	64.17°	308.27°	69.2°	36.8°	M81-338	−80.89°	−22.25°	−67.0°	29.2°
FHB	62.00°	310.32°	66.6°	38.1°	M79-336	−79.68°	−24.12°	−66.0°	29.3°
NAQ	61.16°	314.56°	65.0°	42.3°	M78-337	−77.52°	−23.42°	−64.3°	30.7°

Note. Corrected geomagnetic (CGM) coordinates were calculated for epoch 2016 (using http://sdnet.thayer.dartmouth.edu/aacgm/aacgm%5Fcalc.php%23AACGM).

after application of a 10-point smoothing to reduce noise and eliminate isolated bad data points, the data were numerically differentiated using the three-point Lagrangian approximation. Plots of the time series of data and derivatives were produced and saved, and the maximum and minimum derivative values were automatically determined and recorded.

Interplanetary magnetic field data for these studies were taken from three sources: (a) the OMNI database accessed via CDAWEB (https://cdaweb.gsfc.nasa.gov/index.html/), which provides measurements from the L1 upstream libration point after time-shifting to the nose of the bow shock, (b) observations by the Artemis spacecraft (Themis B and C) in orbit around the moon (also accessed via CDAWEB) and c) from the much nearer Geotail spacecraft, in orbit around the Earth (Weygand & McPherron, 2006a, 2006b) and (http://vmo.igpp.ucla.edu/data1/Weygand/PropagatedSolarWindGSM/weimer/Geotail/). Only Artemis and Geotail data verified to be in the solar wind were retained.

3. Case Studies

For each of the events presented in this section, we show a composite figure consisting of 2-hr excerpts of three-axis magnetograms (in local geomagnetic coordinates) from the stations listed above, as well as simultaneous 2-hr plots of the IMF (in GSM coordinates) from the OMNI time-shifted database and a near-Earth monitor (either Geotail or Themis B). Also included at the bottom of each figure is a table listing the largest derivative (in any component, and either positive or negative) at each station during this interval, and an orange circle on the corresponding plot indicates the time of its occurrence. For each event, we also note the timing of its occurrence relative to a recent geomagnetic storm (if any) and in Table 2 we list the most recent prior substorms (if any), as compiled in three substorm lists (Forsyth et al., 2015; Newell & Gjerloev, 2011; Ohtani & Gjerloev, 2020) available on the SuperMAG web site (https://supermag.jhuapl.edu/substorms/).

Table 2
The Universal Times of Substorm Onsets Identified Within 2 hr Prior to or During the Four Case Studies Presented in Section 3

Date	UT	YRDAY	N & G 2011	F 2015	O & G 2020
14 April 2016	21:00	16,105	1912, 1957, 2022, 2043	1957, 2029	None
6 January 2016	01:00	16,006	0032, 0057	0002	(2347)
6 March 2016	22:30	16,066	2124, 21:58	2125	None
11 May 2016	01:00	16,132	None	(2304), 0058	(2326)

Note. Times in parentheses are from the previous day. N & G 2011: Newell and Gjerloev, (2011) F 2015: Forsyth et al. (2015), O & G 2020: Ohtani and Gjerloev (2020)

Data obtained during the first event exhibited very similar magnetic perturbations and derivatives with comparable amplitudes in the northern and southern polar regions. During the second and third events much stronger perturbations and derivatives appeared in one hemisphere. The fourth event exhibited more complex patterns.

3.1. 14 April 2016

Figure 2 shows IMF and high latitude magnetometer data from 20:00 to 22:00 UT 14 April 2016, with the interval from 20:40 to 21:20 UT highlighted. Column (a) shows time-shifted IMF data in GSM coordinates from OMNI and Geotail, respectively. The three columns at the right show magnetic field components from (b) South Pole Station and BAS-LPM stations M85, M84, and M83; (c) AAL-PIP stations PG2, PG3, PG4, and PG5; and (d) Greenland West Coast stations UMQ, GDH, STF, and SKT. Traces from these stations are arranged vertically in order of magnetic latitude. The vertical arrow in column (b) indicates that the *Bx* trace from M83 has been shifted to lower latitude to not overlap the M84 trace.

The initial negative turnings of the *Bx* component near 20:43 UT were nearly simultaneous at the lowest latitude stations in both hemispheres in all three columns (b–d). The *Bx* minima were strongest between 70° and 72° MLAT. Perturbations in *By* and *Bz* had opposite signs in the two hemispheres. As noted by Engebretson et al. (2020), the relative orientations of the *Bx* and *By* perturbations most likely reflect the hemispheric difference in the circular Hall current flow around a localized field-aligned current (FAC), counterclockwise in the Northern Hemisphere and clockwise in the Southern Hemisphere.

The largest ΔBx perturbations were similar and their minima occurred within ~3 min of each other near 20:52 UT at latitudinally conjugate stations in Antarctica (PG4 and PG5) and Greenland (STF and SKT). They were smaller and occurred later at the higher latitude stations (PG2, PG3, UMQ, and GDH). These differences show both the localized nature of the GMDs and the often-observed poleward motion of the structures that generate these events, as noted earlier in case studies presented by Engebretson, Steinmetz, et al. (2019). Similar or slightly weaker ΔBx perturbations appeared at corresponding times at the BAS-LPM stations to the west.

Figure S1 in the Supporting Information S1 shows the derivatives observed at each available station during this event, in a format similar to that of the corresponding panels in Figure 2. Although there was a general similarity between the amplitudes of the ΔB components and of the derivatives, they were not strictly proportional. (Note that for 14 April 2016, BAS M84 data was only available at 10-s resolution, so the derivatives are smaller.) This lack of proportionality in amplitude has been noted in several earlier studies as well (Engebretson, Pilipenko, et al., 2019; Viljanen, 1997; Viljanen et al., 2006). It can also be seen that the largest derivatives appeared on the falling or rising slopes of the ΔBx perturbations, not at their minima or maxima, and thus did not occur at the same times.

This event occurred at the end of the main phase of a geomagnetic storm (minimum SYM/H = −67 nT). The solar wind velocity (Vsw) was ~410 km/s, the solar wind dynamic pressure (Psw) was ~2.2 nPa, and the AL and AU magnetic indices were ~−500 and ~250 nT, respectively. Three prior substorm onsets between 20:20 and 20:30 UT were identified on this day (Table 2), but none of them appeared in all three substorm lists, and it is not clear that the GMD onset near 20:50 UT was closely related to any of them. (It is important to note that the Ohtani and Gjerloev (2020) list only includes isolated substorms.)

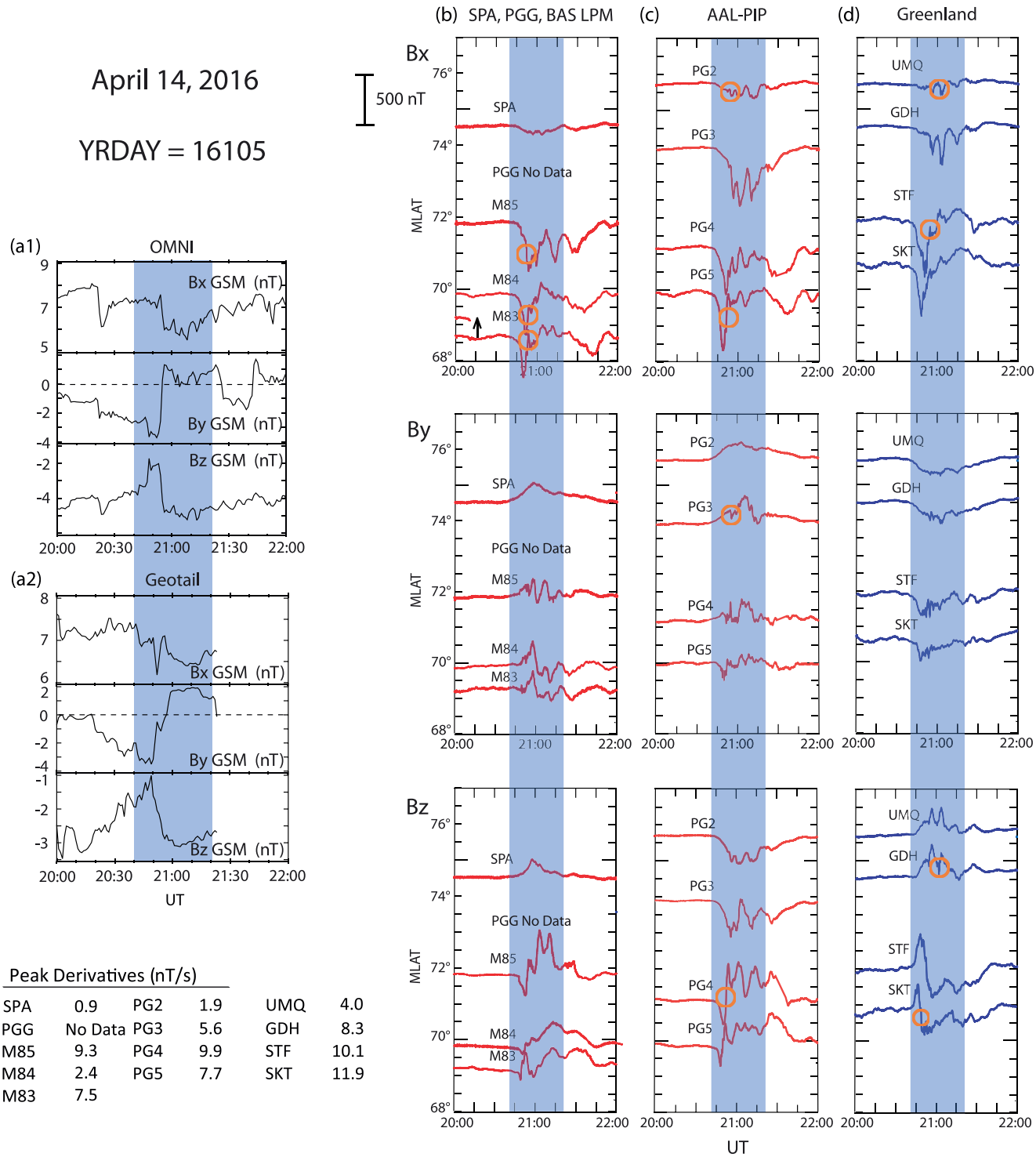

Peak Derivatives (nT/s)

SPA	0.9	PG2	1.9	UMQ	4.0
PGG	No Data	PG3	5.6	GDH	8.3
M85	9.3	PG4	9.9	STF	10.1
M84	2.4	PG5	7.7	SKT	11.9
M83	7.5				

Figure 2. Composite figure showing interplanetary magnetic field (IMF) and high latitude magnetometer data from 20:00 to 22:00 UT 14 April 2016. Column (a) shows IMF data in GSM coordinates from the OMNI database and Geotail. The three columns at the right show magnetic field components in local geomagnetic coordinates from (b) South Pole Station and BAS-LPM stations M85, M84, and M83; (c) AAL-PIP stations PG2, PG3, PG4, and PG5; and (d) Greenland West Coast stations UMQ, GDH, STF, and SKT. Traces from these stations are arranged vertically in order of magnetic latitude. A small orange circle is located near the largest derivative at each station. Also shown at the bottom left is the peak derivative amplitude (in any component) at each station. The vertical arrow in column (c) indicates that the *Bx* trace from M83 has been shifted to lower latitude in order to not overlap the M84 trace.

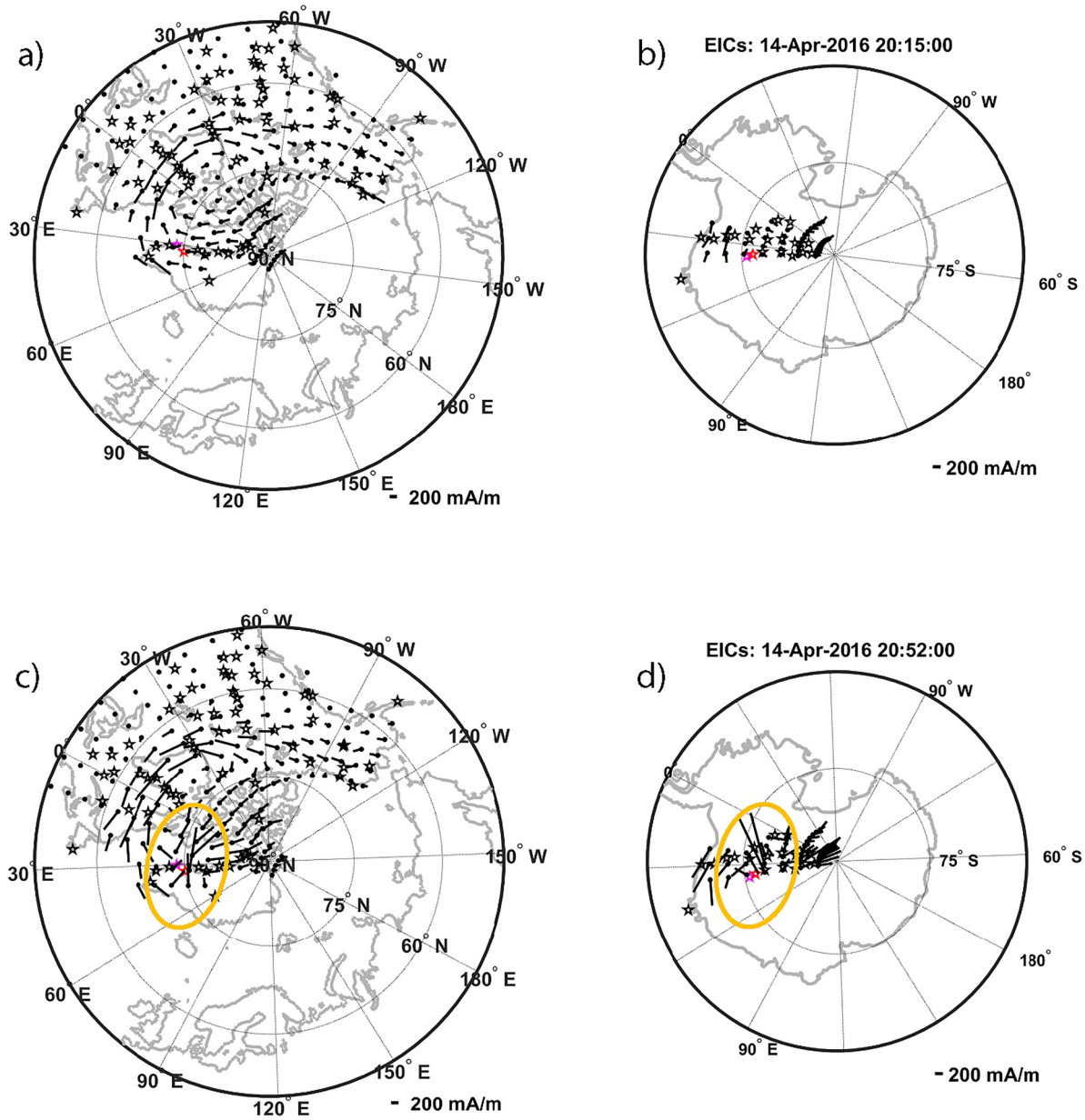

Figure 3. Equivalent ionospheric currents produced using the Spherical Elementary Current Systems method for both the northern and southern hemispheres at two times: at 20:15 UT (panels a and b) and 20:52 UT (panels c and d). The left (right) panels display the northern (southern) hemisphere currents plotted over the landmasses (gray curve) in a magnetic coordinate system with magnetic noon at the top, dawn on the right side, dusk on the left side, and magnetic midnight at the bottom. Mauve colored stars show the location of the SKT (north) and PG5 (south) conjugate station pair, and red colored stars the location of the STF (north) and PG4 (south) conjugate station pair. The orange ovals in panels c and d indicate the regions in each hemisphere surrounding these two conjugate pairs, at which strong and latitudinally localized currents appeared.

In the OMNI data shown in panel a1, IMF *Bz* rose from −3 to −2 nT coincident with the beginning of the GMD at 20:50 UT and returned to −5 nT at 20:55 UT. In the near-Earth Geotail data shown in panel a2, *Bz* rose more gradually from −3 to −1 nT during the interval before returning to −3 nT after 20:50 UT. In both OMNI and Geotail data the *By* component fell gradually until ∼20:51 UT, shortly before the time of GMD onset, and then rose rapidly past 0 near 20:55 UT.

Figure 3 shows equivalent ionospheric currents produced using the Spherical Elementary Current Systems (SECS) method (Weygand, 2009; Weygand et al., 2011) for both the northern and southern hemispheres at two times: at 20:15 UT during the geomagnetically quiet period before the GMD (panels a and b), and at 20:52 UT, during the time of the strongest magnetic perturbations at the lower latitude stations (panels c and d). The left

(right) panels display the northern (southern) hemisphere currents plotted over the landmasses (gray curve) in a magnetic coordinate system with magnetic noon at the top, dawn on the right side, dusk on the left side, and magnetic midnight at the bottom. The dots mark where the equivalent current has been derived and the vector indicates the magnitude and direction of the current. The stars indicate stations with available and valid data for this date. The amplitude key for the currents is in the lower right corner of each panel.

In panel (a) a portion of the dusk side convection cell is apparent and the throat of the cusp starts just north of the Northwest Territories. The eastward electrojet crosses over Hudson Bay and the east coast of Canada. Panel (b) shows the equivalent ionospheric currents in the southern hemisphere over a limited region. The southern hemisphere is shown as a glass earth projection so magnetic noon is at the top, dawn on the right side, dusk on the left side, and magnetic midnight at the bottom. Because of the limited magnetometer coverage in Antarctica only a small portion of the eastward electrojet is visible near Coats Land, Antarctica. Panels (c and d) display the equivalent ionospheric currents during the GMD event at 20:52 UT. In general, in the Northern hemisphere all the currents are significantly larger, the duskside convection cell is still present, and the throat of the cusp is not readily apparent most likely because IMF By is about −3 nT. The orange ovals in panels (c and d) show the region where the GMD was located: Mauve colored stars show the location of the SKT (north) and PG5 (south) conjugate station pair, and red colored stars the location of the STF (north) and PG4 (south) conjugate station pair. The GMD is visible in the lower latitude portion of Greenland around magnetometer stations STF and SKT as equivalent ionospheric currents pointing toward the sun. The GMD is also apparent in Antarctica near stations PG4 and PG5 as equivalent ionospheric currents pointing toward the sun.

The SECS technique also identified pairs of upward and downward currents (a proxy for FACs) in both hemispheres. Figure S2 in the Supporting Information S1 shows that these currents were much weaker over western Greenland and the Antarctic AAL-PIP and BAS-LPM arrays at 20:15 UT than at 20:52 UT, the time of the GMD event. At 20:52 UT an upward current appeared south of STF and a downward current north of it. Similarly, a downward current appeared above and south (poleward) of PG3 and an upward current north (equatorward) of it. Applying the right-hand rule to the Pedersen current connecting the two vertical current pairs reproduces the westward equivalent current seen in Figures 3c and 3d. However, because of the paucity of magnetometer coverage east and west of these arrays, we cannot determine the longitudinal extent of the inferred FACs or the location of their epicenters.

3.2. 6 January 2016

Figure 4 shows IMF and high latitude magnetometer data from 00:00 to 02:00 UT 6 January 2016 with the interval between 00:30 and 01:30 UT highlighted. This geomagnetically quiet interval (Dst = +12) occurred 6 days after the most recent geomagnetic storm. The solar wind velocity (Vsw) was ∼500 km/s, the solar wind dynamic pressure (Psw) was ∼5.52 nPa, and the AL and AU magnetic indices were ∼−700 and ∼100 nT, respectively. Several substorm onsets (Table 2) were noted prior to or during this interval (very differently in the three lists), but only the one at 00:57 UT appeared to closely precede the GMDs.

Sharp drops in *Bx* appeared near 00:37 UT at STF and SKT in Greenland, simultaneous with weak inflections at PG4 in Antarctica, the more poleward Greenland stations GDH and UMQ, and PGG in Arctic Canada. Sharp drops at these four latter stations appeared near 00:57 UT. Short-lived transient perturbations can be seen to occur within the subsequent negative bays at each of these stations, culminating in final large spikes near 01:25 UT, but perturbations were larger in all three components at all northern hemisphere stations than at southern hemisphere stations at comparable latitudes. Perturbations farther west, at PGG, appeared to be intermediate in amplitude but slightly delayed in time relative to those at comparable latitudes in Greenland. In contrast, variations at SPA, PG2, and PG3 during this interval were very weak. Perturbations in *Bx* at Antarctic stations at lower latitude (M85, M84, M83, and PG4) were similar to but weaker than those at STF and SKT, and their perturbations in the *By* and *Bz* components were again significantly weaker.

Figure S3 in the Supporting Information S1 shows the derivatives observed at each available station during this event, in a format similar to that of the corresponding panels in Figure 4. During this event derivatives at each of the northern hemisphere stations remained at elevated levels for time intervals ranging from ∼30 to ∼60 min.

Both the OMNI and Geotail data showed that during the highlighted interval the IMF *Bz* component was again mostly negative but that the IMF *By* component was positive. The *By* magnitude was larger than the *Bz* magnitude in OMNI data but similar in Geotail data.

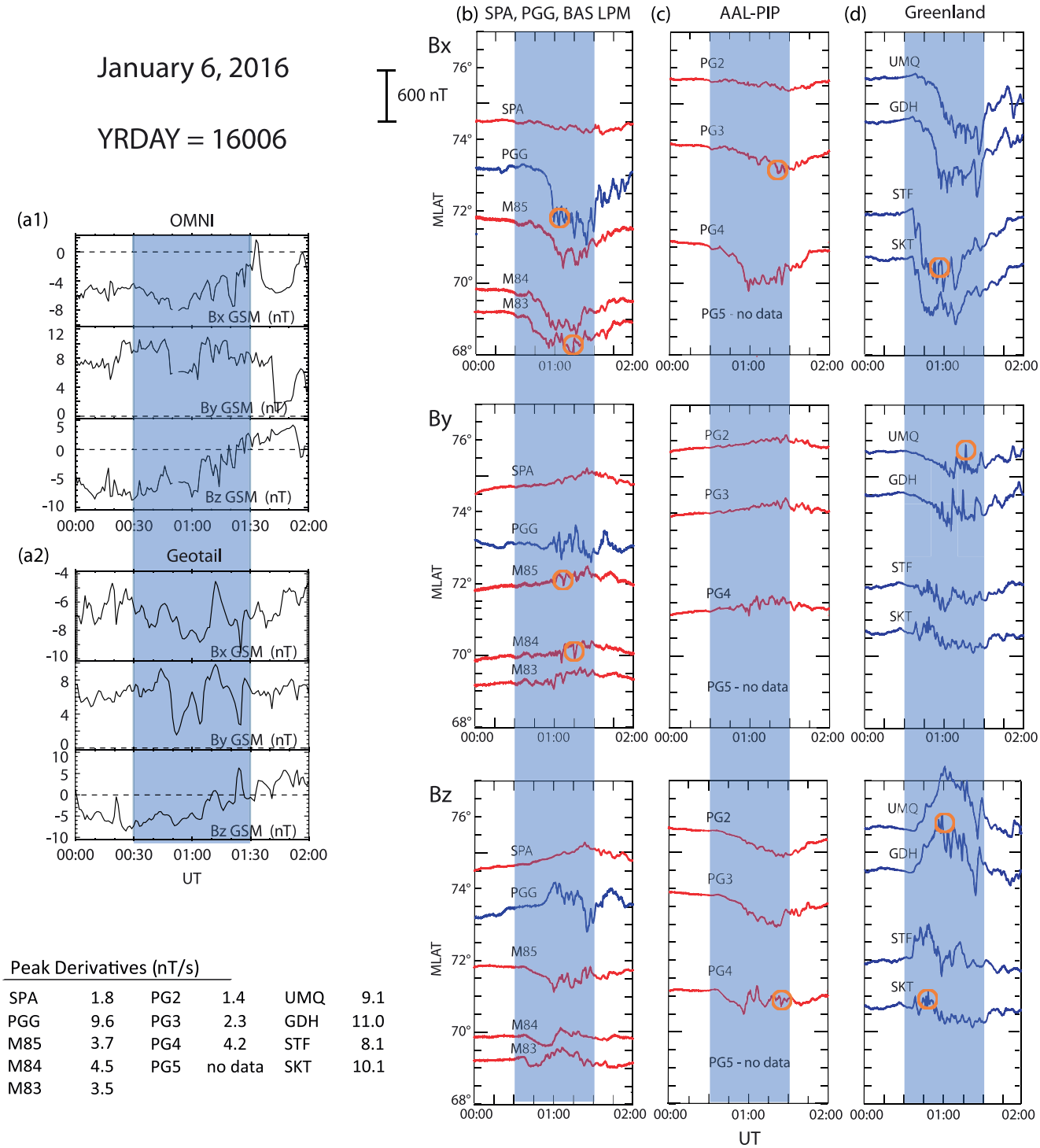

Peak Derivatives (nT/s)

SPA	1.8	PG2	1.4	UMQ	9.1
PGG	9.6	PG3	2.3	GDH	11.0
M85	3.7	PG4	4.2	STF	8.1
M84	4.5	PG5	no data	SKT	10.1
M83	3.5				

Figure 4. Composite figure showing interplanetary magnetic field (IMF) and high latitude magnetometer data from 00:00 to 02:00 UT 6 January 2016, as in Figure 2. A small orange circle is located near the largest derivative (if >2 nT/s) at each station.

3.3. 6 March 2016

Figure 5 shows IMF and high latitude magnetometer data from 21:30 to 23:30 UT 6 March 2016 with the interval between 22:00 and 22:45 UT highlighted. This interval coincided with the end of the main phase of a strong geomagnetic storm (Dst = −98 nT). The solar wind velocity (Vsw) was ~500 km, the solar wind dynamic

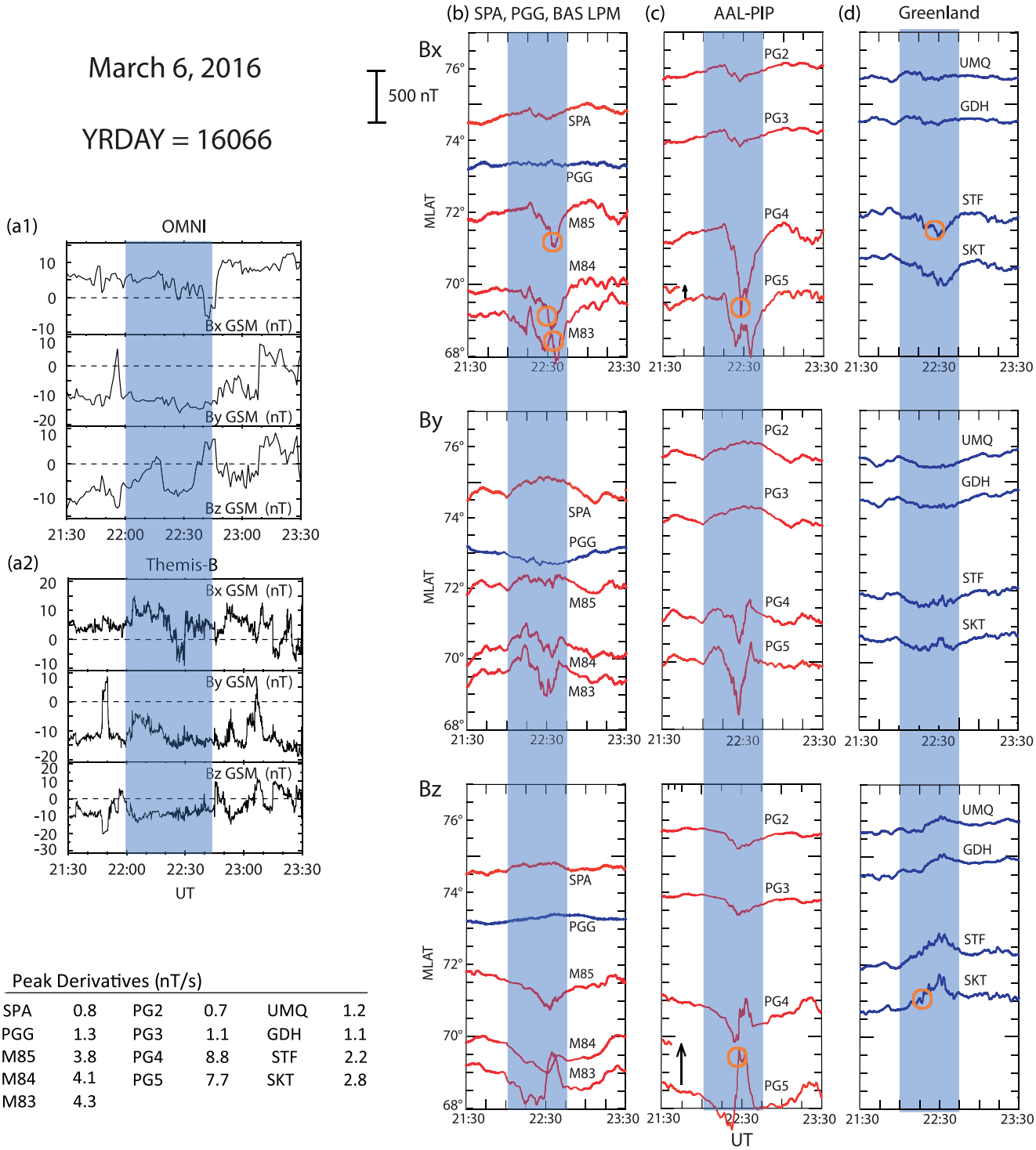

Peak Derivatives (nT/s)

SPA	0.8	PG2	0.7	UMQ	1.2
PGG	1.3	PG3	1.1	GDH	1.1
M85	3.8	PG4	8.8	STF	2.2
M84	4.1	PG5	7.7	SKT	2.8
M83	4.3				

Figure 5. Composite figure showing interplanetary magnetic field (IMF) and high latitude magnetometer data from 21:30 to 23:30 UT 6 March 2016, as in Figure 2. Column (a) shows IMF data in GSM coordinates from the OMNI database and Themis B. A small orange circle is located near the largest derivative (if > 2 nT/s) at each station. The vertical arrows in panel (c) indicate that the *Bx* and *Bz* traces from PG5 have been shifted to lower latitude in order to not overlap the PG4 traces.

pressure (Psw) was ~8 nPa, and the AL and AU magnetic indices were ~ −700 and ~150 nT, respectively. Several substorm onsets were noted prior to or during this interval (very differently in the three lists); the onset at 21:58 occurred just before the beginning of the highlighted interval, but none of the onsets occurred within the interval.

Only very small perturbations and derivatives appeared at the higher latitude Antarctic stations SPA, PG2, and PG3 and at the higher latitude Greenland stations PGG, UMQ, and GDH, consistent with a storm-induced equatorward expansion of the auroral oval. Large perturbations and derivatives appeared at Antarctic stations M85, M84, M83, PG4, and PG5, but only much smaller perturbations and derivatives appeared at Greenland stations STF and SKT. We also note that the Bx minima at PG4 and STF occurred nearly simultaneously.

Figure S4 in the Supporting Information S1 shows the derivatives observed at each available station during this event, in a format similar to that of the corresponding panels in Figure 5. Only shorter intervals of elevated derivatives appeared at the more equatorward stations in the southern hemisphere, but with clear enhancements in the *X* and *Y* components nearly simultaneously at PG4 and PG5.

Both the OMNI and Themis B data showed that during the highlighted interval the IMF *By* component was strongly negative (near −10 nT). The IMF *Bz* component in Themis B data was negative but relatively steady and smaller, near −7 nT, and the OMNI *Bz* component was near −7 nT between 22:48 and 22:35 but slightly positive before and after that interval. During this event Themis B was located upstream and on the dawnside of Earth, at Rx = 49 R_E, Ry = −27 R_E, and Rz = 3 R_E in GSE coordinates. Geotail was in the magnetosphere during this interval.

3.4. 11 May 2016

Figure 6 shows IMF and high latitude magnetometer data from 00:00 to 02:00 UT 11 May 2016 with two short intervals highlighted: 00:40 to 01:05 UT and 01:10 to 01:20 UT. This moderately disturbed interval (Dst = −28) occurred on the fourth day of recovery after a strong geomagnetic storm with minimum Dst = −88. The solar wind velocity (Vsw) was ∼550 km/s, the solar wind dynamic pressure (Psw) was ∼0.8 nPa, and the AL and AU magnetic indices were ∼−250 and ∼140 nT, respectively. Table 2 shows that two substorm onsets occurred during the final hour of the previous day (May 10), and one onset (included only in the Forsyth et al. list) occurred at 00:58 UT.

There was considerable magnetic activity throughout this 2-hr period, but it was generally weaker than in the three previous examples (note the smaller scale of the vertical axis during this event). During the first highlighted interval large magnetic bays appeared at the lower latitude Antarctic stations M85, M84, M83, PG3, PG4, and PG5, with narrow spikes in several components at 01:00 UT at M83 (9.8 nT), PG4 (5.8 nT), and PG5 (5.8 nT). Much weaker bays and spikes appeared at SPA and PG2, and very little activity appeared at UMQ and GDH. Slightly stronger variations appeared at STF and SKT, with a narrow spike only in the *Bz* component at SKT (4.6 nT). During the second highlighted interval negative bays were evident only at SPA and more weakly at PGG, but large derivatives appeared at many stations that showed little evidence of negative bays. Large narrow spikes with large derivatives appeared in all three components at 01:15 UT at STF (8.0 nT) and SKT (5.1 nT), and much smaller peaks appeared in *Bz* at UMQ and GDH. Spikes of moderate to large derivative amplitude also appeared simultaneously at 01:15 UT in one or more components at PG3 (5.3 nT), PG4 (3.7 nT), and PG5 (3.0 nT), and in the higher latitude range to the west in both hemispheres, at SPA (5.6 nT), PGG (5.0 nT), and M85 (2.0 nT).

Figure S5 in the Supporting Information S1 shows the derivatives observed at each available station during this event, in a format similar to that of the corresponding panels in Figure 6. This event included a mixture of isolated derivative peaks, most noticeable in data from M84 and M83 at 01:00 UT and at STF and SKT at 01:15 UT, and more extended intervals with smaller but still elevated derivative amplitudes.

IMF data from OMNI and Geotail were not only variable but showed significant disagreement during this two-hour interval, as did also the data from the three L1 monitors. In particular, during the first shaded interval the *Bz* component observed by OMNI was >0 between 00:40 and 00:54 UT before dropping to ∼−1 nT at 01:00 UT, while the *Bz* component observed by Geotail was negative throughout. The *By* component in OMNI data was near 0 until 01:00 UT, while the By component in Geotail data was near 1 nT until 01:05 UT. During the second interval the observed *Bz* traces varied in opposite directions. The *Bz* component in OMNI data was near −1 nT at 01:10 UT, but rose to near 0 after 01:14 UT. The *Bz* component in Geotail data was near +0.3 nT at the beginning of this interval and dropped to negative values (∼−1 nT) after 01:15 UT. The *By* components in OMNI and Geotail data remained mostly negative during this second interval, but again varied in opposite direc-

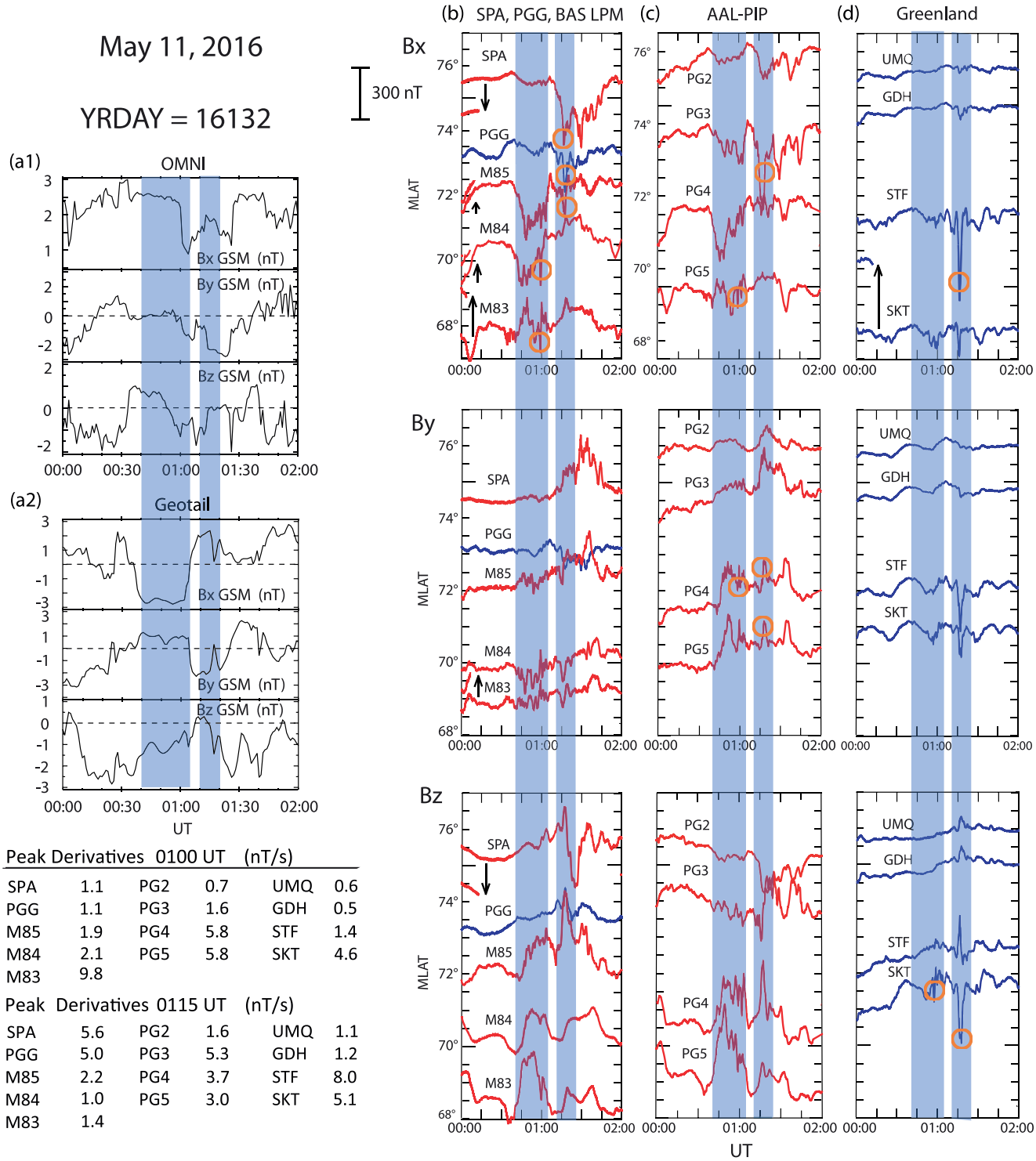

Peak Derivatives 0100 UT (nT/s)

SPA	1.1	PG2	0.7	UMQ	0.6
PGG	1.1	PG3	1.6	GDH	0.5
M85	1.9	PG4	5.8	STF	1.4
M84	2.1	PG5	5.8	SKT	4.6
M83	9.8				

Peak Derivatives 0115 UT (nT/s)

SPA	5.6	PG2	1.6	UMQ	1.1
PGG	5.0	PG3	5.3	GDH	1.2
M85	2.2	PG4	3.7	STF	8.0
M84	1.0	PG5	3.0	SKT	5.1
M83	1.4				

Figure 6. Composite figure showing interplanetary magnetic field (IMF) and high latitude magnetometer data from 00:00 to 02:00 UT 11 May 2016, as in Figure 2. Column (a) shows IMF data in GSM coordinates from the OMNI database and Geotail. A small orange circle is located near the largest derivative (if > 2 nT/s) at each station. The vertical arrows in panels (b) and (d) indicate that some of the traces from SPA, M83, and SKT have been shifted in latitude in order to not overlap the adjacent traces. Note also the different latitudinal (vertical) scale for the *Bx* part of panel (b) than for panels (c) and (d).

Table 3
Summary of the Four Case Study Events

Date	Storm phase	Recent prior substorms	AL, AU	IMF *By*	Amplitude ratio	Close Δ*Bx* timing
14 April	End of Main	Y	500, 250 nT	~0	N~S	Y
6 January	Recov. Day 6	Y	700, 100 nT	+6 nT	N >> S	?
6 March	End of Main	Y	770, 150	–10 nT	S > N	Y
11 May	Recov. Day 4	Y	250, 140 nT	Mixed	Mixed	Y

tions. Figure S6 in the Supporting Information S1 shows that the three upstream solar wind monitors orbiting the L1 Langrangian point were located ~250 R_E upstream from Earth, but were considerably off the Sun-Earth line (WIND −96 R_E, DSCOVR −22 R_E, and ACE +24 R_E in the Y_{GSE} direction, respectively). Panels (c–e) show that the IMF observed during the shaded intervals at the three spacecraft also showed significant variability and differences in all three components.

Note especially the isolated spike at many stations near 01:16 UT that was nearly simultaneous at many stations both N and S. It was not associated with any significant magnetic bay at most stations, so was presumably caused by a very localized set of ionospheric and/or field-aligned currents.

Table 3 summarizes the characteristics of the case study events, including the occurrence of nearly simultaneous conjugate *ΔBx* minima. The variety in IMF *By* polarity and geomagnetic activity will be considered in the next section.

4. Statistical Studies

A total of 66 separate >6 nT/s GMDs were identified at one or more of the stations in the four Greenland-Antarctica station pairs listed above during the first 6 months of 2016. A large majority of these exceeded 6 nT/s at one or both stations in more than one station pair. In the few cases during which more than one >6 nT/s GMD was identified at a given station during a given 2 hr UT interval, only the largest amplitude event was counted.

Columns 2 and 4 of Table 4 list the number of GMDs with derivatives >6 nT/s in any component at the northern and southern hemisphere station in each station pair, respectively. Columns 6–10 show the number of events at each station pair with one or two exceeding the 6 nT/s threshold, and their sum and ratio, respectively. It is clear that more >6 nT/s events appeared at the two lower latitude station pairs (45 and 55) than at the two higher latitude pairs (19 and 34). This latitudinal pattern is similar to that found in Table 2 of Engebretson, Pilipenko et al. (2021) for stations at comparable magnetic latitudes in eastern Arctic Canada.

4.1. Seasonal Trend

Figure 7 shows the ratio of derivatives at northern and southern stations $(dB_N/dt)/(dB_S/dt)$, for each of the four conjugate station pairs as a function of the day of the year in 2016. Each panel shows only those events with at least one >6 nT/s event at each station pair. A linear fit to the base 10 logarithm of the ratios as a function of

Table 4
Number of >6 nT/s GMDs Recorded at Four Stations Each in the Greenland West Coast Magnetometer Chain and in the AAL-PIP Magnetometer Chain

Station Greenland	Events >6 nT/s	Station Antarctica	Events >6 nT/s	Station pair	Events >6 nT/s per Pair			Ratio
					1 per pair	2 (both)	Total	2 ev/1 ev
UMQ	11	PG2	11	UMQ-PG2	16	3	19	0.19
GDH	18	PG3	23	GDH-PG3	27	7	34	0.26
STF	24	PG4	34	STF-PG4	32	13	45	0.41
SKT	29	PG5	42	SKT-PG5	39	16	55	0.41

Note. Station Events Station Events Station Pair Events >6 nt/s per Pair Ratio.

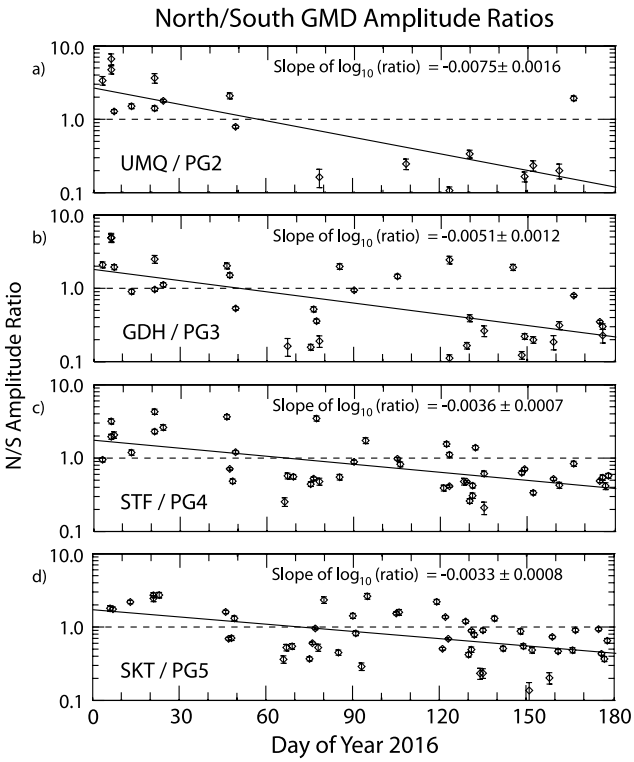

Figure 7. Plot of the ratio of GMD derivatives at northern and southern stations, $dB_N/dt/dB_S/dt$, as a function of the day of the year in 2016 for each of the four conjugate station pairs: (a) UMQ/PG2, (b) GDH/PG3, (c) STF/PG4, and (d) SKT/PG5. Only those events with at least one >6 nT/s event at each station pair are shown.

day of the year is also shown. There is considerable scatter in each plot (to be discussed in Section 5.1), but the lines fit the distributions reasonably well (there is little evidence for a nonlinear relation), and the majority of the events have error bars (based on the documented noise level of the magnetometers in each array) of roughly the same size as the plotting symbols. Documentation for the error bar calculations is provided in the Supporting Information S1. These panels clearly show a seasonal dependence on the slope; it is roughly twice as steep for the highest latitude UMQ/PG2 pair as for the lowest latitude SKT/PG5 pair.

4.2. IMF *By* Dependence

In an attempt to identify a source for the scatter in each of the amplitude ratio plots in Figure 7, we next examined the IMF *Bz* and *By* components (using both OMNI and Artemis/Themis time-shifted IMF data as available) to determine their values prior and up to the time of GMD occurrences. Of the 66 GMDs, 47 (71%) were preceded by an interval of at least 15 min of IMF $Bz < 0$, while five were preceded by IMF $Bz > 0$, and another 14 by intervals with mixed IMF *Bz* polarity. However, only 34 of the 47 GMDs with consistently negative IMF *Bz* values had a consistent IMF *By* value (+, within 1 nT of 0, or −) during this same interval. Figure 8 shows the GMD amplitude ratios for the STF/PG4 station pair following these intervals of consistently negative IMF *Bz* and consistent IMF *By* values. Events with $By > 1$ nT are shown in blue, *By* within 1 nT of 0 in red, and $By < -1$ in green. Panels (a and b) show all events for which OMNI data and Artemis/Themis IMF data satisfied these conditions, respectively, and panel (c) shows only those events for which OMNI and Artemis/Themis data both saw consistent IMF $Bz < 0$ and the same category of consistent IMF *By* values. Plots for the other station pairs are shown as Figures S7–S9 in the Supporting Information S1. The patterns shown are consistent with a small IMF *By* effect (N/S ratio larger for $By > 1$ than for $By < -1$) that is convolved with a seasonal effect, but there is considerable overlap, and the numbers of $By > 1$ and *By* near 0 events are very small.

Table 5 shows the results of a regression analysis to test the difference between the means of the $By > 1$ and $By < -1$ GMD amplitude ratio distributions for each of the four station pairs. The seasonal trend was removed by including day of year as a covariate in this analysis. (These seasonal trends are shown in Figure 7.) The few $By \sim 0$ events were not included in this analysis. Mean differences were calculated for the mean date of observations at each station while accounting for the seasonal trend. The differences in the means were statistically significant for all four station pairs, using either OMNI or Artemis/Themis IMF data. The slopes of the regression lines in Figure 7 were also significantly different from zero (all p values < 0.05; p value $= 0.002$ for UMQ, all other p values < 0.001). The remaining large scatter in the values of individual ratios, however, cannot be explained by either seasonal or IMF *By* effects or, as noted above, by instrumental measurement errors.

4.3. Time Delay Analysis

The addition of stations somewhat west of the Greenland—AAL-PIP conjugate arrays in the case studies above gave little direct evidence for any IMF *By*-induced longitudinal skewing in opposite hemispheres. It also became apparent while surveying all the GMDs in this data set that in many cases the waveforms of the *Bx* (north-south) component at conjugate stations were roughly simultaneous (the two minima occurred within 3 min of each other). Events with such near simultaneity were also noted in Figures 2, 5, and 6. In order to further investigate the conditions leading to close timing between conjugate hemispheres, we determined the time of each ΔBx minimum to within ±1 s by successively zooming in on magnetograms of each of the GMD events at each station in the three lowest latitude station pairs.

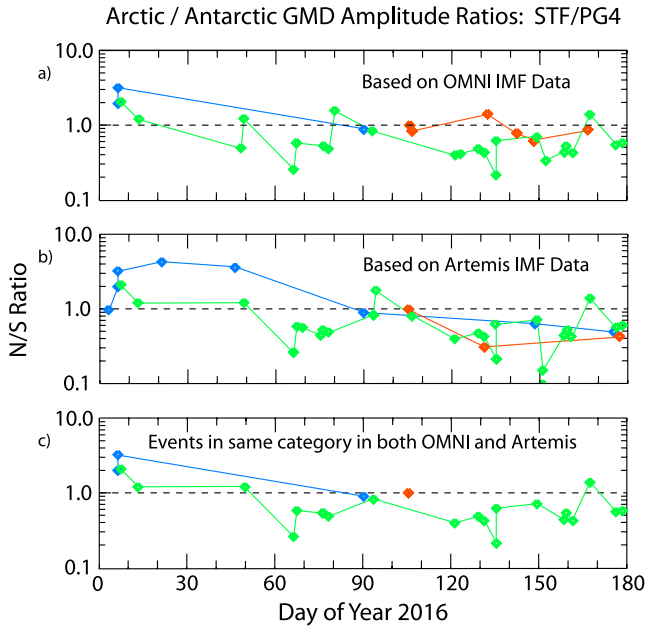

Figure 8. Plots of the ratios of amplitudes of GMD events observed at the STF/PG4 conjugate station pair during events preceded by an interval of at least 15 min of interplanetary magnetic field (IMF) $Bz < 0$ and IMF By being consistently either >1 nT (blue), within 1 nT of 0 (red), or <−1 (green). Panels (a) and (b) show all events for which OMNI data and Artemis/Themis IMF data satisfied these conditions, respectively, and panel (c) shows only those events for which OMNI and Artemis/Themis data saw both consistent IMF $Bz < 0$ and the same category of consistent IMF By values.

Figure 9 shows the distribution of time delays (positive values are associated with later event times in the north than in the south) for the STF-PG4 station pair. The relative timing error is ±2 s, much less than the size of the diamond symbols. What stands out in all three sets are that there are two populations: one with $|T_N - T_S| < 3$ min, and the other with larger time differences, ranging from ~5 to ~30 min. All nine distributions in Figure 9 are dominated by events with time delays clustered within 3 min of 0, but also show a small number of events with much larger delays. In each of the three panels IMF $By > 1$ events are skewed slightly to the left and IMF $By < -1$ events are skewed to the right. In the bottom panel, however, using only those events for which Themis and OMNI IMF observations agreed, the pattern was more consistent: $By > 0$ to the left, $By \sim 0$ near 0, and $By < 0$ to the right with only one exception. Figures for the GDH-PG3 and SKT-PG5 station pairs showing similar distributions are shown as Figures S10 and S11 in the Supporting Information S1.

Figure 10 provides a comparison of the distributions from all three of these station pairs, but combines events in all three IMF By categories in one histogram. Events were strongly peaked near 0 at each station pair and in both data sets, but with a slight skewing toward more positive values in the OMNI data compared to the Artemis/Themis data. The few large time lags in either direction occurred most often in the STF-PG4 data set.

In order to better characterize the dependence of $T_N - T_S$ on the IMF $By/|Bz|$ ratio, Figure 11 shows a plot of time differences $T_N - T_S$ as a function of the IMF $By/|Bz|$ ratio component in Artemis/Themis data for those GMD events in the data set used for Figure 8 and Figures S7, S9 in the Supporting Information S1 with consistent IMF $Bz < 0$ and the same category of consistent IMF By values (>1 nT, near 0, or <1 nT) during an interval of at least 15 min prior to an event, but now excluding cases when By changed sign during this interval. This resulted in a further reduction in the number of events and reduced even further the number of events with $By > 0$. Because of the small number of events, this plot includes all events at three conjugate station pairs (GDH-PG3, STF-PG4, and SKT-PG5). Table 6 provides information on the number of events at each of the three station pairs, indicating that for 77% of these events the Bx minima occurred within 3 min of each other.

The accuracy of the times of Bx minima at each station, determined from high resolution plots with a range of 1 min, was usually <±1 s. The accuracy of each $T_N - T_S$ value is thus usually ±2 s, a value much smaller than the plot symbols. Errors in IMF By and Bz were derived from visual estimates of half the distance from the mean to either approximate extreme during the 15 min prior to the GMD. These values were then used to calculate the errors in the IMF $By/|Bz|$ ratio. The resulting error limits ranged from ±0.3 to ±1.5.

Table 5
ANCOVA Test of the Difference Between the Means of the By > 0 and By < 0 GMD Amplitude Ratios for Each of the Four Station Pairs After Removal of the Effects of the Linear Seasonal Variations

	OMNI	Artemis
Station pair	Average difference at mean date	Average difference at mean date
UMQ/PG2	2.523[a] ± 1.135	1.612[a] ± 0.974
GDH/PG3	1.777[a] ± 1.049	1.124[a] ± 0.701
STF/PG4	0.926[a] ± 0.642	0.932[a] ± 0.614
SKT/PG5	0.760[a] ± 0.602	0.539[a] ± 0.419
All station pairs	1.591[a] ± 0.464	1.069[a] ± 0.342

[a]Statistically significant (p value < 0.05).

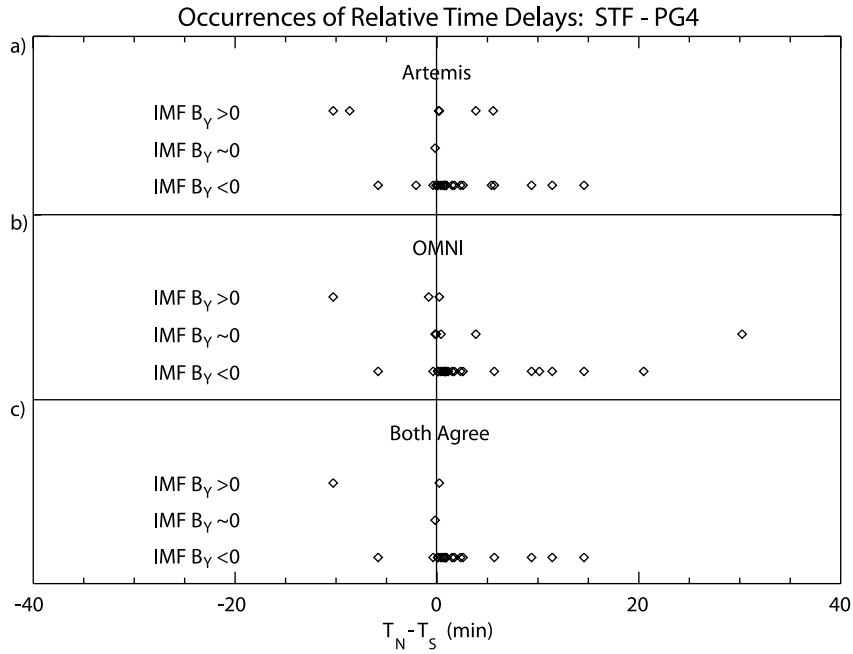

Figure 9. Plots of the distribution of time delays ($T_N - T_S$) between observations of the ΔBx minima associated with each GMD event in at the STF-PG4 station pair. Panel (a) shows events with interplanetary magnetic field (IMF) $By > 1$, within ± 1 of 0, and < -1, respectively, as measured by Artemis/Themis. Panel (b) shows events measured by OMNI, and panel (c) shows only those events for which Artemis/Themis and OMNI IMF categories agreed.

The division into two populations noted above is evident in Figure 11: most have time delays between −3 and +3 min, and a much smaller number have delays from 3 to 15 min. There is no evident dependence on the By / $|Bz|$ ratio for the events between −3 and +3 min; the events in this population have a remarkably flat distribution. It is also evident that most of the events in Figure 11 are in the left half. This again reflects the strong skewing of all large GMD events in this data set to be associated with intervals of negative IMF By. Although the distribution of events with time delays above 3 min in Figure 9 are skewed slightly to the left for $By > 1$ events and to the right for $By < -1$ events, and Figure 11 gives evidence of a relation between the polarity of the IMF By component and the relative time delay between northern and southern conjugate stations, their number is so small and the IMF ratio errors so large that any slope determined from these data is not statistically significant. We also looked for a seasonal trend in the time delays, but no pattern was evident for either extreme or modest time differences.

5. Discussion

This paper has compared observations of large magnetic perturbation events at high northern and southern latitudes to better understand their similarities and differences at magnetically conjugate high latitude sites. We have identified a clear seasonal variation and a somewhat weaker dependence on the sign of the By component of the IMF, using data from the OMNI data base (using data from the L1 upstream libration point that has been time-shifted to the nose of the bow shock), from the Artemis/Themis spacecraft (in orbit about the Moon, again after time-shifting), and from the Geotail spacecraft (in orbit about Earth). None of these three provided useable data for all the events cataloged during the first 6 months of 2016, and in a considerable number of cases the available IMF data exhibited at least minor differences.

The 11 May 2016 event is one of several exceptions to the general pattern of N/S derivative amplitude ratio depending on the sign of IMF By. Given the observed amplitudes of perturbations in the two shaded intervals, one might expect either small or negative IMF By at 01:00 UT and either small or positive IMF By at 01:15, along with a negative IMF Bz. It is possible that neither IMF data set correctly shows the IMF data that impinged on the magnetosphere during this interval.

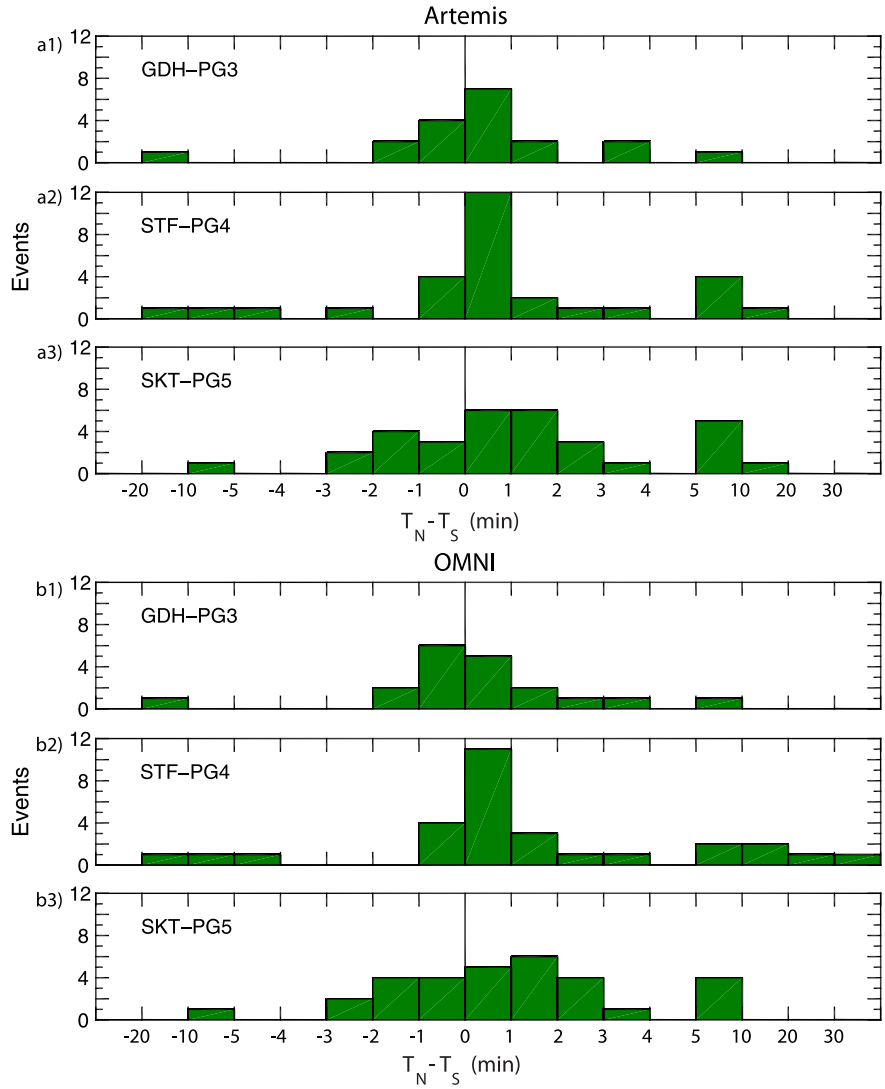

Figure 10. Histograms of the north-south time delay between GMD events observed at magnetically conjugate station pairs GDH-PG3, STF-PG4, and SKT-PG5, using events in all three categories of interplanetary magnetic field (IMF) *By* from (a) Artemis/Themis data and (b) OMNI data. Note the larger bin sizes beyond ±5 min.

Determining the character of the IMF that actually impinges on Earth's magnetosphere presents many challenges, as noted by Weimer et al. (2002), Borovsky (2018), and Burkholder et al. (2020) and exemplified in a study of Pc 3–4 waves by Bier et al. (2014). In both our case studies and statistical studies, we have presented data using IMF data from both OMNI and a nearer-Earth monitor. These have produced modest but recognizable differences in the resulting patterns in amplitudes, but have led to similar statistical conclusions regarding the influence of seasonal and IMF *By* effects on the ratios of amplitudes at conjugate stations. Even in combination these influences are insufficient to remove most of the scatter in these ratios. A check of the values of the IMF magnitude and solar wind velocity and pressure for each event revealed no additional pattern of influence external to the magnetosphere that would explain the remaining scatter in conjugate amplitudes.

5.1. Amplitude Comparisons

The control of GMD amplitude by IMF *By* reported here is consistent with the results of several earlier studies. Holappa et al. (2021b) noted that many studies using ground magnetometers, beginning with Friis-Christensen and Wilhjelm (1975) and using polar-orbiting satellites (Friis-Christensen et al., 2017; Smith et al., 2017), have shown that auroral electrojets in the northern hemisphere winter are stronger in both hemispheres for $By > 0$ than

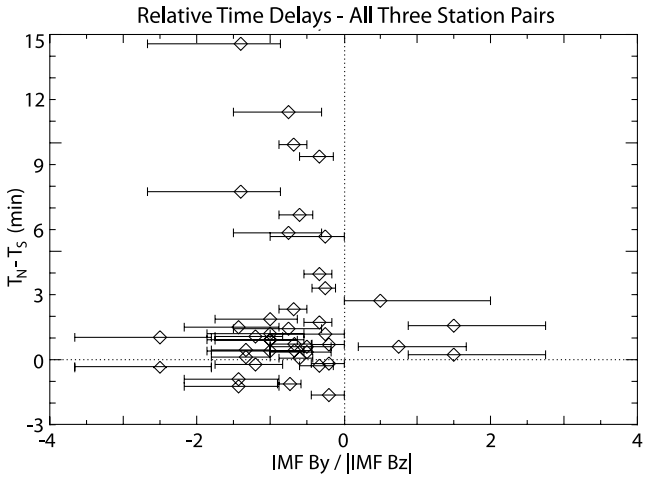

Figure 11. Plot of the time delay $T_N - T_S$ between minima in the *Bx* component at three conjugate station pairs (GDH-PG3, STF-PG4, and SKT-PG5) as a function of the IMF *By*/*Bz* ratio for all events where the signs of the IMF *Bz* and *By* components in the Artemis and OMNI data bases agreed.

for $By < 0$, and that in NH summer the dependence on the *By* sign is reversed. Holappa et al. (2021b) noted that this *By* sign dependence is very strong in the winter hemisphere, but it is weak in the summer hemisphere, and is much stronger in the westward electrojet than in the eastward electrojet. Holappa and Buzulokova (2022) noted that the physical mechanisms of IMF *By* effects, which apply not only to auroral zone electron precipitation and ionospheric conductance but also to the fluxes of energetic magnetosphere protons and the growth rate of the ring current, are still not fully understood.

In addition, Workayehu et al. (2021), using nearly 6 years of magnetic field measurements from the Swarm A and C satellites, reported that auroral currents were stronger in the northern hemisphere than the southern hemisphere for IMF $By > 0$ in most local seasons under both signs of IMF *Bz*. This pattern provides an explanation for the distribution of IMF orientations in the ecliptic plane shown in the Engebretson, Ahmed et al. (2021) superposed epoch study of GMDs observed in Arctic Canada, because the northern hemisphere values would be stronger for $By > 0$, so more likely to exceed the 6 nT/s amplitude threshold. The distributions of IMF *Bx* and *By*, shown separately in Figure 9 of that paper, included both positive and negative values, but the median in *Bx* was <0 and that in *By* was >0, consistent with a Parker-spiral oriented IMF vector directed toward Earth. Figure S7 in the Supporting Information S1 of that paper, showing the medians of the *x*–*y* vector component of the IMF, revealed that a Parker-Spiral vector directed Earthward (with $By > 0$) was observed consistently for premidnight events occurring less than 30 min after the most recent substorm onset (panels a1–a5), and was often observed also during most premidnight events occurring between 30 and 60 min after substorm onset (panels b1–b5). However, the directions and sign of the *By* component were much more varied and at times had ortho-Parker-Spiral orientation for postmidnight events. (It is notable that no postmidnight GMDs during the first half of 2016 satisfied the selection criteria for the present study.)

Our observations of a strong seasonal dependence regardless of the sign of IMF *By* appear to be somewhat inconsistent with the IMF *By* polarity dependence in these earlier studies. However, Workayehu et al. (2021) also reported a complex dependence on season, and it is conceivable that the seasonal dependence evident in our data set might be restricted to the longitude region and/or 6 month period where these observations were made.

A subsequent study by Holappa et al. (2021a) found that the substorm onset latitude and the isotropic boundary latitude of energetic protons were both ~1° lower during IMF $|By| > 3$ conditions than for smaller *By*, and that the substorm occurrence frequency was larger for small |*By*|. They suggested, consistent with the results of a resistive MHD study by Hesse and Birn (1990), that the magnetotail was more stable during conditions of large IMF |*By*|, requiring the magnetotail lobes and the polar cap to contain more flux to initiate a substorm compared to the situation when |*By*| was small. Our observations that GMDs were strongly suppressed under IMF conditions dominated by the *By* component (Engebretson, Ahmed, et al., 2021) and occurred only when preceded by intervals of IMF $Bz < 0$ and conditions when |IMF *By*| < 2 |IMF *Bz*| (this study) suggests that their generation is in some way linked to magnetotail reconnection.

Table 6
The Number of GMDs With Time Differences Between Bx Minima of <3 and >3 min, Respectively, for Three Arctic-Antarctic Station Pairs

T_{diff}	GDH-PG3	STF-PG4	SKT-PG5	Total	Total %
$\|\Delta t\| < 3$	7	13	13	33	77
$\|\Delta t\| > 3$	2	4	4	10	23
Total Events	9	17	17	43	100

Note. Events were restricted to those for which the IMF had a fairly steady *By*/*Bz* ratio in Artemis/Themis data during the 15 min prior to the GMD and the Artemis/Themis and OMNI data agreed on their signs.

A probable explanation for the remaining scatter in amplitude ratios that is independent of seasonal or IMF *By*-related factors is based on the horizontal dimensions of the GMDs and of the effective separation (from ~150 to ~300 km) and range of sensitivity of ground-based magnetometers. Chinkin et al. (2021), using data from the IMAGE magnetometer network, reported that magnetic field variations associated with GICs had a spatial scale of a few hundred km, consistent with estimates of the horizontal half-amplitude radius of the GMDs reported by Engebretson, Pilipenko et al. (2019) and Engebretson, Steinmetz et al. (2019) of ~275 km, and by Weygand et al. (2021) of ~250–450 km, with a somewhat greater longitudinal extent in some cases. The sensitivity of a ground magnetometer to ionospheric

currents varies as the inverse square of the distance from the magnetometer on the ground to the current in the overhead ionosphere (~100–150 km altitude), and thus also falls off rapidly as the horizontal separation exceeds 200–300 km. If the center of an event fell within 200–300 km of both the northern and southern "conjugate" stations, both stations would see the same event with little additional difference in amplitude. If the horizontal distance between the center of a GMD and only one ground magnetometer site exceeded 200–300 km, this would produce an additional reduction in the measured amplitude at that station.

5.2. Relative Timing

We have also noted that GMDs observed in conjugate hemispheres very often occurred nearly simultaneously (within <3 min) regardless of IMF *By* polarity as long as $|By| < \sim 2|Bz|$. Many satellite imaging studies reviewed by Ohma et al. (2018) using simultaneous observations of similar auroral features in both hemispheres have shown that they are displaced longitudinally when IMF $By \neq 0$, such that when IMF $By > 0$ structures appear in the southern auroral zone up to ~2 hr MLT later than in the north (i.e., shifted eastward), and vice versa for IMF $By < 0$. Østgaard et al. (2011b), using data from several years of conjugate auroral observations from the IMAGE and Polar spacecraft, found a sinusoidally varying mean longitudinal displacement at substorm onset between the two hemispheres that maximized near ±0.5 hr MLT at IMF clock angles of 90° and 270°, respectively, and an event study by Reistad et al. (2016) showed displacements of up to 3 hr MLT.

However, substorms have been observed to rapidly decrease this displacement. Østgaard et al. (2011a) found that the conjugate auroral features became more similar in MLT during the expansion phase of two substorms. Throughout the first substorm the IMF was stable and *By* dominated, so they concluded that the longitudinal displacement was removed by processes related to the magnetospheric substorm. Ohma et al. (2018) subsequently presented 10 case studies confirming that a reduction in the longitudinal displacement was a common signature of substorms: the aurora became more north-south symmetric in 8–30 min, which is similar to the typical duration of the substorm expansion phase, and the rate of change was related to the reconnection rate.

As noted in earlier studies by Engebretson, Pilipenko, et al. (2021) and Engebretson, Ahmed, et al. (2021), the majority of >6 nT/s GMDs most often occurred within 30 min after substorm onsets (but only very rarely coinciding with them), although many others occurred long after the onset of any prior substorm. If GMDs are triggered by reconnection in the magnetotail, as appears likely, then this close agreement in *Bx* minima associated with GMDs should also be expected for events occurring shortly after a substorm onset, as happened prior to all four of the case study events presented above, but a time shift should be expected for events occurring after extended intervals of lesser geomagnetic activity.

The 10 events shown in Figure 11 with $T_N - T_S > 3$ min (appearing later in the north) were all associated with IMF $By < 0$. This is consistent with the shift in auroral longitudes observed by Østgaard et al. (2011a) and Ohma et al. (2018). The values of the AL index 1 hr before the occurrence of the GMDs shown in Figure 11 provide additional evidence suggesting consistency with their findings. The values of the AL index 1 hr before the 10 GMD events with $T_N - T_S > 3$ ranged from −10 to −350 nT, with a mean of −117 nT and a median of −105 nT, characteristic of relatively quiet conditions. In contrast, the AL values during the 33 events with $|T_N - T_S| < 3$ min ranged from −40 to −460 nT, with a mean of −191 nT and a median of −180 nT, indicating somewhat more disturbed conditions.

The relative timing pattern noted here is also subject to observational uncertainties, however. The magnetic conjugacy between locations in Antarctica and Greenland is known to vary with season and dipole tilt as well as with magnetic activity, which in turn is parameterized in empirical magnetic field models by magnetic indices and the components of the IMF. According to their nominal corrected geomagnetic latitudes, GHB (69.2°) is slightly closer to the conjugate latitude of PG5 (−69.9°) than is SKT (70.7°) and SKT is slightly closer to the conjugate latitude of PG4 (−71.2°) than is STF (71.9°). Using the T89 model to trace the field lines of the West Greenland stations to the surface of Antarctica, at 21:00 UT on 14 April 2016 (using $K_p = 3.333$) SKT was magnetically very close to PG5 and PG4 was at the same magnetic latitude as STF but shifted westward, consistent with the pairing used to determine amplitude ratios above. However, at 01:00 UT on 11 May 2016 (using $K_p = 2.0$), GHB was magnetically very close to PG5 and SKT was very close to PG4. Given these K_p values, higher latitude stations were near or outside the region of closed field lines, so no conjugate tracing using the T89 model was possible.

Table 7
The Number of GMDs With Time Differences Between Bx Minima <3 and >3 min, Respectively, for Four Arctic-Antarctic Station Pairs

T_{diff}	SKT-PG5	GHB-PG5	STF-PG4	SKT-PG4
$\|\Delta t\| < 3$	41	21	35	38
$\|\Delta t\| > 3$	14	20	17	18
Total Events	55	41	52	56

Note. Events with isolated minima are included here regardless of IMF orientations.

Motivated by the variation in conjugacy indicated by these model results, we have calculated the timing differences between the GMD *Bx* minima for the GHB-PG5 and SKT-PG4 station pairs in order to compare them with SKT-PG5 and STF-PG4 station pairs. Table 7 shows the number of events with the differences between *Bx* minima >3 and < 3 min for each of these pairs, using all 66 events regardless of IMF conditions but excluding those events at which multiple closely spaced minima appeared at one or both stations. The number of events in the GHB-PG5 column was reduced because no data were available from GHB between 22 May and 2 June.

Table 7 shows that the number of *Bx* minima simultaneous to within 3 min was more than double the number with larger time delays for three of the four station pairs. The numbers for GHB-PG5 were almost equal, and the reason for this discrepancy is not clear. These comparisons suggest that despite the modest shifts in conjugacy expected between hemispheres at these high magnetic latitudes, the similarities and differences reported in Section 4 above appear to be reasonably consistent.

6. Conclusions

Using the only currently available conjugate high latitude magnetometer arrays, we have investigated the conjugacy of large transient geomagnetic disturbances that, if they occurred over more technologically developed regions, would generate large GICs. Four case studies have demonstrated some of the similarities and differences between GMD events in conjugate hemispheres, and by using 6 months of magnetic field data from four conjugate station pairs in West Greenland and Antarctica in combination with measurements of the IMF, we have been able to quantify their dependence on season and IMF *Bz* and *By* polarity. Uncertainty in the IMF dependences stems from the still-limited number of events, the high variability of the IMF, and disagreements between currently available sources of IMF data due to the lack of consistent measurements near the Earth-Sun line and near Earth. In addition, some of the variability in the timing of conjugate GMDs may be due to the inaccuracy and variability of conjugate mappings between hemispheres.

1. We have found that IMF *Bz* was <0 shortly during the 15 min preceding and/or during a large majority (71%) of these events (as in our other recent studies). This suggests but cannot strongly confirm the influence of reconnection in the magnetotail as a link in the causal chain leading to these events.
2. Two factors appeared to exert modest control over the relative amplitude of GMDs in the northern and southern polar regions.
   (a) The N/S amplitude ratio was increased when IMF *By* > 0, and decreased when IMF *By* < 0.
   (b) Latitudinal/seasonal dependences caused GMDs to have larger amplitudes in the winter hemisphere; larger seasonal differences were observed at higher latitudes.
3. The remaining differences in amplitude may well be due to the convolution of the spatial localization of the ionospheric currents that cause these events and the horizontal range of detection of these currents by ground-based magnetometers. A dense, two-dimensional array in at least one hemisphere may be needed in order to counter the combined effects of small-scale size of nighttime GMDs and the dynamically varying points of magnetic conjugacy at these high latitudes in order to diminish the large event-to-event variability evident in this data set.
4. The relative timing between conjugate GMDs (the majority of them simultaneous to within ±3 min) was consistent both with the sense of longitudinal shift in auroral features revealed in earlier studies of simultaneous satellite images (Figure 9), and with the rapid reduction in these shifts during substorms. The addition of stations somewhat west of the West Greenland—AAL-PIP conjugate arrays in the case studies gave no evidence for any IMF *By*-induced longitudinal skewing in opposite hemispheres, consistent with the close temporal connection of many of these events to prior substorm activity.
5. GMDs were observed in conjugate hemispheres regardless of IMF *By* polarity as long as $|By| < \sim 2|Bz|$. As noted by Engebretson, Ahmed, et al. (2021), a separate study of 156 intervals in 2015 when the IMF was dominated by large *By* values found that only one of these coincided with a GMD in the northern hemisphere. This suggests that GMD occurrences are suppressed by large and dominant IMF *By* values.

Much work remains to be done before the dependences on external factors identified here can be accurately characterized. The statistical associations found here between GMD occurrences and prior intervals of IMF $Bz < 0$ and IMF *By* of either sign are insufficient to quantify any possible IMF-related delay time until GMD onset, in part because of the limitations of the IMF data bases themselves. In addition, the physical processes leading to GMDs are still only poorly understood. The fact that they occur not only during geomagnetically disturbed conditions but also during relatively quiet times suggests that although they are likely to be caused by instabilities in the magnetotail, ground-satellite conjunction studies at various tailward distances appear to necessary in order to characterize, and even more so to predict, the occurrence of the mesoscale or small-scale events that trigger them.

Data Availability Statement

OMNI Solar wind and IMF data are available at the Goddard Space Flight Center Space Physics Data Facility at http://mist.nianet.org/, as are also IMF data from the Artemis/Themis spacecraft and from the Greenland West Coast magnetometer chain. AAL-PIP magnetometer data are available in CDF and IDL save set formats at http://mist.nianet.org/ and in ASCII format at https://cdaweb.gsfc.nasa.gov. MACCS magnetometer data are available in IAGA 2002 ASCII format at http://space.augsburg.edu/maccs/requestdatafile.jsp and in ASCII format at https://cdaweb.gsfc.nasa.gov. South Pole Station magnetometer data are available in ASCII format at https://antarcticgeospace.njit.edu/Data/, and BAS-LPM magnetometer data are available at https://data.bas.ac.uk/metadata.php?id=GB/NERC/BAS/PDC/00848). Geotail propagated data are available at (http://vmo.igpp.ucla.edu/data1/Weygand/PropagatedSolarWindGSM/weimer/Geotail/).

Acknowledgments
This research was supported by NSF Grants AGS-2013648 to Augsburg University, AGS-2013433 to the University of Michigan, PLR-1543364, OPP-1744828, AGS-2027210, and AGS-2027168 to Virginia Tech, and OPP-1643700 to the New Jersey Institute of Technology, and Natural Environment Research Council Grant NE/R016038/1 to the British Antarctic Survey. The spherical elementary currents produced by James M. Weygand were made possible by NASA Grants 80NSSC18K1220, 80NSSC18K1227, 80NSSC20K1364, 80NSSC18K0570, NASA Contract 80GSFC17C0018, and NSF GEO-NERC 2027190.

References

Bier, E. A., Owusu, N., Engebretson, M. J., Posch, J. L., Lessard, M. R., & Pilipenko, V. A. (2014). Investigating the IMF cone angle control of Pc3-4 pulsations observed on the ground. *Journal of Geophysical Research: Space Physics*, *119*, 1797–1813. https://doi.org/10.1002/2013JA019637

Borovsky, J. E. (2018). The spatial structure of the oncoming solar wind at Earth and the shortcomings of a solar-wind monitor at L1. *Journal of Atmospheric and Solar-Terrestrial Physics*, *177*, 2–11. https://doi.org/10.1016/j.jastp.2017.03.014

Boteler, D. H. (2001). Assessment of geomagnetic hazard to power systems in Canada. *Natural Hazards*, *23*, 101–120. https://doi.org/10.1023/A:1011194414259

Boteler, D. H. (2019). A 21st century view of the March 1989 magnetic storm. *Space Weather*, *17*, 1427–1441. https://doi.org/10.1029/2019SW002278

Boteler, D. H., Pirjola, R. J., & Nevanlinna, H. (1998). The effects of geomagnetic disturbances on electrical systems at the Earth's surface. *Advances in Space Research*, *22*, 17–27. https://doi.org/10.1016/S0273-1177(97)01096-X

Burkholder, B. L., Nykyri, K., & Ma, X. (2020). Use of the L1 constellation as a multispacecraft solar wind monitor. *Journal of Geophysical Research: Space Physics*, *125*, e2020JA027978. https://doi.org/10.1029/2020JA027978

Chinkin, V. E., Soloviev, A. A., Pilipenko, V. A., Engebretson, M. J., & Sakharov, Y. A. (2021). Determination of vortex current structure in the high-latitude ionosphere with associated GIC bursts from ground magnetic data. *Journal of Atmospheric and Solar-Terrestrial Physics*, *212*, 105514. https://doi.org/10.1016/j.jastp.2020.105514

Clauer, C. R., Kim, H., Deshpande, K., Xu, Z., Weimer, D., Musko, S., et al. (2014). An autonomous adaptive low-power instrument platform (AAL-PIP) for remote high-latitude geospace data collection. *Geoscientific Instrumentation, Methods and Data Systems*, *3*, 211–227. https://doi.org/10.5194/gi-3-211-2014

Engebretson, M. J., Ahmed, L. Y., Pilipenko, V. A., Steinmetz, E. S., Moldwin, M. B., Connors, M. G., et al. (2021). Superposed epoch analysis of nighttime magnetic perturbation events observed in Arctic Canada (2021). *Journal of Geophysical Research: Space Physics*, *126*, e2021JA029465. https://doi.org/10.1029/2021JA029465

Engebretson, M. J., Araki, T., Arnoldy, R. L., Carpenter, D. L., Doolittle, J. H., Fukunishi, H., et al. (1997). The United States automatic geophysical observatory (AGO) program in Antarctica. In M. N. W. Lockwood, & H. J. Opgenoorth (Eds.), *The satellite-ground based coordination sourcebook*, (pp. 65–99). Noordwijk, Netherlands: ESTEC, ESA Publications.

Engebretson, M. J., Hughes, W. J., Alford, J. L., Zesta, E., Cahill, L. J., Jr., Arnoldy, R. L., & Reeves, G. D. (1995). Magnetometer array for cusp and cleft studies observations of the spatial extent of broadband ULF magnetic pulsations at cusp/cleft latitudes. *Journal of Geophysical Research*, *100*, 19371–19386. https://doi.org/10.1029/95JA00768

Engebretson, M. J., Kirkevold, K. R., Steinmetz, E. S., Pilipenko, V. A., Moldwin, M. B., McCuen, B. A., et al. (2020). Interhemispheric comparisons of large nighttime magnetic perturbation events Relevant to GICs. *Journal of Geophysical Research: Space Physics*, *125*, e2020JA028128. https://doi.org/10.1029/2020JA028128

Engebretson, M. J., Pilipenko, V. A., Ahmed, L. Y., Posch, J. L., Steinmetz, E. S., Moldwin, M. B., et al. (2019). Nighttime magnetic perturbation events observed in Arctic Canada: 1. Survey and statistical analysis. *Journal of Geophysical Research: Space Physics*, *124*, 7442–7458. https://doi.org/10.1029/2019JA026794

Engebretson, M. J., Pilipenko, V. A., Steinmetz, E. S., Moldwin, M. B., Connors, M. G., Boteler, D. H., et al. (2021). Nighttime magnetic perturbation events observed in Arctic Canada: 3. Occurrence and amplitude as functions of magnetic latitude, local time, and magnetic disturbances. *Space Weather*, *19*, e2020SW002526. https://doi.org/10.1029/2020SW002526

Engebretson, M. J., Steinmetz, E. S., Posch, J. L., Pilipenko, V. A., Moldwin, M. B., Connors, M. G., et al. (2019). Nighttime magnetic perturbation events observed in Arctic Canada: 2. Multiple-instrument observations. *Journal of Geophysical Research: Space Physics*, *124*, 7459–7476. https://doi.org/10.1029/2019JA026797

Forsyth, C., Rae, I. J., Coxon, J. C., Freeman, M. P., Jackman, C. M., Gjerloev, J., & Fazakerley, A. N. (2015). A new technique for determining substorm onsets and phases from indices of the electrojet (SOPHIE). *Journal of Geophysical Research: Space Physics*, *120*, 10592–10610. https://doi.org/10.1002/2015JA021343

Friis-Christensen, E., Finlay, C. C., Hesse, M., & Laundal, K. M. (2017). Magnetic field perturbations from currents in the dark polar regions during quiet geomagnetic conditions. *Space Science Reviews*, *206*(1–4), 281–297. https://doi.org/10.1007/s11214-017-0332-1

Friis-Christensen, E., & Wilhjelm, J. (1975). Polar cap currents for different directions of the interplanetary magnetic field in the Y-Z plane. *Journal of Geophysical Research*, *80*(10), 1248–1260. https://doi.org/10.1029/JA080i010p01248

Gannon, J. L., Swidinsky, A., & Xu, Z. (Eds.) (2019). Geomagnetically induced currents from the Sun to the power grid. *Geophysical Monograph Series* (Vol. 244). American Geophysical Union. https://doi.org/10.1002/9781119434412

Hapgood, M. (2019). The Great storm of May 1921: An exemplar of a dangerous space weather event. *Space Weather*, *17*, 950–975. https://doi.org/10.1029/2019SW002195

Hesse, M., & Birn, J. (1990). Magnetic reconnection in the magnetotail current sheet for varying cross-tail magnetic field. *Geophysical Research Letters*, *17*(11), 2019–2022. https://doi.org/10.1029/GL017i011p02019

Holappa, L., & Buzulukova, N. Y. (2022). Explicit IMF By-dependence of energetic protons and the ring current. *Geophysical Research Letters*, *49*, e2022GL098031. https://doi.org/10.1029/2022GL098031

Holappa, L., Reistad, J. P., Ohma, A., Gabrielse, C., & Sur, D. (2021a). The magnitude of IMF by influences the magnetotail response to solar wind forcing. *Journal of Geophysical Research: Space Physics*, *126*, e2021JA029752. https://doi.org/10.1029/2021JA029752

Holappa, L., Robinson, R. M., Pulkkinen, A., Asikainen, T., & Mursula, K. (2021b). Explicit IMF *By*-dependence in geomagnetic activity: Quantifying ionospheric electrodynamics. *Journal of Geophysical Research: Space Physics*, *126*, e2021JA029202. https://doi.org/10.1029/2021JA029202

Kadokura, A., Yamagishi, H., Sato, N., Nakano, K., & Rose, M. C. (2008). Unmanned magnetometer network observation in the 44th Japanese Antarctic Research Expedition: Initial results and an event study on auroral substorm evolution. *Polar Science*, *2*, 223–235. https://doi.org/10.1016/j.polar.2008.04.002

Knipp, D. J. (2015). Synthesis of geomagnetically induced currents: Commentary and research. *Space Weather*, *13*, 727–729. https://doi.org/10.1002/2015SW001317

Knipp, D. J., & Gannon, J. L. (2019). The 2019 National Space Weather strategy and action plan and beyond. *Space Weather*, *17*, 794–795. https://doi.org/10.1029/2019SW002254

Lanzerotti, L. J., Wolfe, A., Trivedi, N., Maclennan, C. G., & Medford, L. V. (1990). Magnetic impulse events at high latitudes: Magnetopause and boundary layer plasma processes. *Journal of Geophysical Research*, *95*, 97–107. https://doi.org/10.1029/JA095iA01p00097

Love, J. J., Hayakawa, H., & Cliver, E. W. (2019). Intensity and impact of the New York Railroad superstorm of May 1921. *Space Weather*, *17*, 1281–1292. https://doi.org/10.1029/2019SW002250

Marshall, R. A., Smith, E. A., Francis, M. J., Waters, C. L., & Sciffer, M. D. (2011). A preliminary risk assessment of the Australian region power network to space weather. *Space Weather*, *9*, S10004. https://doi.org/10.1029/2011SW000685

Molinski, T. S., Feero, W. E., & Damsky, B. L. (2000). Shielding grids from solar storms. *IEEE Spectrum*, *37*(11), 55–60. https://doi.org/10.1109/6.880955

Newell, P. T., & Gjerloev, J. W. (2011). Evaluation of SuperMAG auroral electrojet indices as indicators of substorms and auroral power. *Journal of Geophysical Research*, *116*, A12211. https://doi.org/10.1029/2011JA016779

Ngwira, C. M., & Pulkkinen, A. A. (2019). An introduction to geomagnetically induced currents (2019). In J. L. Gannon, A. Swidinsky, & Z. Xu (Eds.), *Geomagnetically induced currents from the Sun to the power grid, Geophysical Monograph Series* (Vol. 244, pp. 3–13). American Geophysical Union. https://doi.org/10.1002/9781119434412.ch1

Ohma, A., Østgaard, N., Reistad, J. P., Tenfjord, P., Laundal, K. M., Snekvik, K., et al. (2018). Evolution of asymmetrically displaced footpoints during substorms. *Journal of Geophysical Research: Space Physics*, *123*, 10030–10063. https://doi.org/10.1029/2018JA025869

Ohtani, S., & Gjerloev, J. W. (2020). Is the substorm current wedge an ensemble of wedgelets?: Revisit to midlatitude positive bays. *Journal of Geophysical Research: Space Physics*, *125*, e2020JA027902. https://doi.org/10.1029/2020JA027902

Østgaard, N., Humberset, B. K., & Laundal, K. M. (2011a). Evolution of auroral asymmetries in the conjugate hemispheres during two substorms. *Geophysical Research Letters*, *38*, L03101. https://doi.org/10.1029/2010GL046057

Østgaard, N., Laundal, K. M., Juusola, L., Åsnes, A., Haaland, S. E., & Weygand, J. M. (2011b). Interhemispherical asymmetry of substorm onset locations and the interplanetary magnetic field. *Geophysical Research Letters*, *38*, L08104. https://doi.org/10.1029/2011GL046767

Reistad, J. P., Østgaard, N., Tenfjord, P., Laundal, K. M., Snekvik, K., Haaland, S. E., et al. (2016). Dynamic effects of restoring footpoint symmetry on closed magnetic field lines. *Journal of Geophysical Research: Space Physics*, *121*, 3963–3977. https://doi.org/10.1002/2015JA022058

Smith, A. R. A., Beggan, C. D., Macmillan, S., & Whaler, K. A. (2017). Climatology of the auroral electrojets derived from the along-track gradient of magnetic field intensity measured by POGO, Magsat, CHAMP, and Swarm. *Space Weather*, *15*(10), 1257–1269. https://doi.org/10.1002/2017SW001675

Viljanen, A. (1997). The relation between geomagnetic variations and their time derivatives and implications for estimation of induction risks. *Geophysical Research Letters*, *24*, 631–634. https://doi.org/10.1029/97GL00538

Viljanen, A., Tanskanen, E. I., & Pulkkinen, A. (2006). Relation between substorm characteristics and rapid temporal variations of the ground magnetic field. *Annales Geophysicae*, *24*, 725–733. https://doi.org/10.5194/angeo-24-725-2006

Weimer, D. R., Ober, D. M., Maynard, N. C., Burke, W. J., Collier, M. R., McComas, D. J., et al. (2002). Variable time delays in the propagation of the interplanetary magnetic field. *Journal of Geophysical Research*, *107*(A8), 1210. https://doi.org/10.1029/2001JA009102

Weygand, J. M. (2009). *Equivalent ionospheric currents (EICs) derived using the spherical elementary currrent systems (SECS) technique at 10 s resolution in geographic coordinates*. University of California. https://doi.org/10.21978/P8D62B

Weygand, J. M., Amm, O., Viljanen, A., Angelopoulos, V., Murr, D., Engebretson, M. J., et al. (2011). Application and validation of the spherical elementary currents systems technique for deriving ionospheric equivalent currents with the North American and Greenland ground magnetometer arrays. *Journal of Geophysical Research*, *116*, A03305. https://doi.org/10.1029/2010JA016177

Weygand, J. M., Engebretson, M. J., Pilipenko, V. A., Steinmetz, E. S., Moldwin, M. B., Connors, M. G., et al. (2021). SECS analysis of nighttime magnetic perturbation events observed in Arctic Canada. *Journal of Geophysical Research: Space Physics*, *126*, e2021JA029839. https://doi.org/10.1029/2021JA029839

Weygand, J. M., & McPherron, R. L. (2006a). Geotail Low Energy Particle (LEP) experiment data Weimer propagated 60 s resolution in GSM coordinates. https://doi.org/10.21978/P89S5D

Weygand, J. M., & McPherron, R. L. (2006b). Geotail Weimer propagated using CPI 60 s resolution Tri-axial fluxgate magnetometer in GSM coordinates. https://doi.org/10.21978/P8SS5R

Woodroffe, J. R., Morley, S. K., Jordanova, V. K., Henderson, M. G., Cowee, M. M., & Gjerloev, J. (2016). The latitudinal variation of geoelectromagnetic disturbances during large ($Dst \leq -100$ nT) geomagnetic storms. *Space Weather*, *14*, 668–681. https://doi.org/10.1002/2016SW001376

Workayehu, A. B., Vanhamäki, H., Aikio, A. T., & Shepherd, S. G. (2021). Effect of interplanetary magnetic field on hemispheric asymmetry in ionospheric horizontal and field-aligned currents during different seasons. *Journal of Geophysical Research: Space Physics*, *126*, e2021JA029475. https://doi.org/10.1029/2021JA029475